

REY-Th-U Dynamics in the Critical Zone: Combined Influence of Reactive Bedrock Accessory Minerals, Authigenic Phases, and Hydrological Sorting (Mule Hole Watershed, South India)

Jean-Jacques Braun, Jean Riotte, Shrema Battacharya, Aurélie Violette, Priscia Oliva, Jonathan Prunier, Jean-Christophe Maréchal, Laurent Ruiz, Stéphane Audry, S. Subramanian

▶ **To cite this version:**

Jean-Jacques Braun, Jean Riotte, Shrema Battacharya, Aurélie Violette, Priscia Oliva, et al.. REY-Th-U Dynamics in the Critical Zone: Combined Influence of Reactive Bedrock Accessory Minerals, Authigenic Phases, and Hydrological Sorting (Mule Hole Watershed, South India). Geochemistry, Geophysics, Geosystems, 2018, 19 (5), pp.1611-1635. 10.1029/2018GC007453 . hal-02860747

HAL Id: hal-02860747
https://brgm.hal.science/hal-02860747

Submitted on 26 Mar 2021

HAL is a multi-disciplinary open access archive for the deposit and dissemination of scientific research documents, whether they are published or not. The documents may come from teaching and research institutions in France or abroad, or from public or private research centers.

L'archive ouverte pluridisciplinaire **HAL**, est destinée au dépôt et à la diffusion de documents scientifiques de niveau recherche, publiés ou non, émanant des établissements d'enseignement et de recherche français ou étrangers, des laboratoires publics ou privés.

Check for updates

AGU100 ADVANCING EARTH AND SPACE SCIENCE

Geochemistry, Geophysics, Geosystems

RESEARCH ARTICLE
10.1029/2018GC007453

Key Points:
- Clarifying the source to sink behavior of REY-Th-U is important for unraveling Earth surface processes and new ore prospection tools
- Secondary iron oxides are key REY-Th-U carriers in the regolith as well as through adsorption or occlusion
- Hydrological sorting privileges the REY-Th-U export as silts and clays in suspended sediments

Supporting Information:
- Supporting Information S1
- Table S1
- Table S2
- Table S3
- Table S4
- Table S5

Correspondence to:
J.-J. Braun,
jean-jacques.braun@ird.fr

Citation:
Braun, J.-J., Riotte, J., Battacharya, S., Violette, A., Oliva, P., Prunier, J., et al. (2018). REY-Th-U dynamics in the critical zone: Combined influence of reactive bedrock accessory minerals, authigenic phases, and hydrological sorting (mule hole watershed, South India). *Geochemistry, Geophysics, Geosystems*, *19*, 1611–1635. https://doi.org/10.1029/2018GC007453.

Received 25 JAN 2018
Accepted 22 MAR 2018
Accepted article online 7 MAY 2018
Published online 18 MAY 2018

© 2018. American Geophysical Union. All Rights Reserved.

REY-Th-U Dynamics in the Critical Zone: Combined Influence of Reactive Bedrock Accessory Minerals, Authigenic Phases, and Hydrological Sorting (Mule Hole Watershed, South India)

Jean-Jacques Braun[1,2], Jean Riotte[1,3], Shrema Battacharya[4,5], Aurélie Violette[1], Priscia Oliva[1], Jonathan Prunier[1], Jean-Christophe Maréchal[6], Laurent Ruiz[3,7], Stéphane Audry[1], and S. Subramanian[3,8]

[1]Géosciences Environnement Toulouse (Université de Toulouse, CNRS, IRD), Toulouse, France, [2]Institut de Recherches Géologiques et Minières/Centre de Recherches Hydrologiques, Yaoundé, Cameroon, [3]Indo-French Cell for Water Sciences, IISc-IRD Joint International Laboratory, IISc, Bangalore, India, [4]Physical Research Laboratory, Ahmedabad, India, [5]Center for Earth Science, IISc, Bangalore, India, [6]BRGM-Service Eau, Montpellier, France, [7]INRA Agrocampus Rennes, UMR, Sol-Agronomie-Spatialisation, Rennes, France, [8]Materials Engineering Department, IISc, Bangalore, India

Abstract The sources of REY-Th-U and long-term mass balance were assessed in the gneissic tropical forested Critical Zone Observatory of Mule Hole, India. The study relies on the characterization of the solid compartments (bedrock, soils, streambed and suspended sediments), on batch leaching experiments of the parent gneiss and on extractions of cation-exchangeable and iron-related pools of selected soil samples. The REY-Th-U primary reservoir is controlled by monazite, xenotime, thorite, allanite, bastnesite, titanite, apatite, and, to a lesser extent, by zircon. This accessory mineral assemblage was profoundly modified by episodes of metamorphism and hydrothermal activity. Allanite, bastnesite, titanite, and apatite are prone to break down at incipient weathering stage while monazite, xenotime and zircon are resistant minerals. On a long-term basis, REY are roughly inert in the immature saprolite and depleted in the soil cover and are strongly redistributed among secondary phases. LREE and HREY are mainly controlled by poorly crystallized secondary iron oxides and oxyhydroxides, and, to a lesser extent, by secondary phosphates (e.g., rhabdophane). Th, inert in the saprolite, is controlled by well-crystallized secondary iron oxides and oxyhydroxides and likely by secondary thorianite (ThO_2). REY and Th are not easily mobilized during surface processes such as chelation by organic matter and uptake by plants. REY and Th are, by far, exported as suspended sediments associated with iron oxides. The U export by groundwater and suspended sediments dominates over those of streambed sediments and stream.

1. Introduction

The natural High Field Strength Elements (HFSE) actinides (U, Th) and Rare Earth Elements (REEs + Y = REY) are widely used as geochemical tracers in the sedimentary cycle and, thus, to understand the evolution of the Upper Continental Crust (Condie et al., 1995; Nesbitt & Markovics, 1997; Taylor & McLennan, 1985). Based on their radioactive properties and dual behavior during weathering processes (i.e., U soluble as UO_2^{2+} in oxidizing conditions (Langmuir, 1978) and Th inert as ThO_2, i.e., thorianite (Langmuir & Herman, 1980), U and Th are used as chronometer in closed regolith systems (e.g., pedogenic carbonates [Violette et al., 2010b]) and as geochemical tracers for weathering processes in open regolith systems (Balan et al., 2005; Chabaux et al., 2003; Dequincey et al., 2002; Ma et al., 2012; Taboada et al., 2006) and for sediment provenance studies (Taylor & McLennan, 1985). Since, early 90s, the mobility, fractionation and redistribution of REY during in situ chemical weathering of silicate rocks and subsequent river transport are well established. The processes are more efficient during warm and humid weathering conditions (Braun et al., 1993; Ma et al., 2011; Thompson et al., 2013; Vazquez-Ortega et al., 2016; Vázquez-Ortega et al., 2015; Viers & Wasserburg, 2004). Their use as geochemical tracer is recognized for interpreting soil genesis processes (Laveuf & Cornu, 2009) as precipitation of secondary phases according to pH (e.g., phosphates, carbonates, sulphates) either catalyzed by bacterial activity or not (Berger et al., 2014; Braun et al., 1990; Taunton et al., 2000; Zaharescu, 2017), plant recycling (Brioschi et al., 2013; Stille et al., 2006; Tyler, 2004), organic and

inorganic chelation and sorption processes (Davranche et al., 2004, 2011; Pourret et al., 2007a), redoximorphism through the evolution of Ce-anomalies and precipitation of CeO_2 (Braun et al., 1990; Janots et al., 2015), and plagioclase weathering through the evolution of the Eu-anomaly (Panahi et al., 2000).

In crystalline silicate rocks, REY, Th, and U often exist together as major elements in the same accessory minerals (Bea, 1996; Cherniak, 2010; Foerster, 1998a, 1998b), which have importance on the biogeochemical budgets. In regolith and, subsequently, in sediments, the REY-Th-U abundance is thus linked to the weathering susceptibility of the primary accessory mineral suite, the transportation of resistant bearing phases and the ability of authigenic clay and clay minerals to retain those elements (Singh & Rajamani, 2001; Su et al., 2017). Apart from their storage within the lattice of resistant heavy bearing minerals, several physicochemical conditions can act to decrease the HFSE mobility such as: (i) their specific adsorption and even occlusion on/in secondary oxide and oxyhydroxide phases (Duff et al., 2002; Vazquez-Ortega et al., 2016), (ii) their precipitation as authigenic soil phases (Banfield & Eggleton, 1989; Braun et al., 1998a; Janots et al., 2015), and (iii) their adsorption on the negatively-charged soil particles (e.g., clay minerals like kaolinite and smectite) (Coppin et al., 2002). Reversely, the HFSE mobility is enhanced by the presence of organic ligands in the circulating fluids and by the fluctuations of redox conditions (Davranche et al., 2011; Dupré et al., 1999; Gruau et al., 2004; Grybos et al., 2007; Pourret et al., 2007a, 2007b; Viers et al., 1997). The REY-Th-U mobilization, redistribution and fractionation depend also on the degree of weathering (Bao & Zhao, 2008; Sanematsu et al., 2013, 2015). Therefore, unraveling the weathering and provenance using bulk REE composition is still not straightforward. Thus, the REY-Th-U pathways from source to sink, i.e. from weathering/erosion to hydraulic sorting, need to be further understood from a mineralogical and geochemical point of view (Su et al., 2017). Moreover, the grade in REE deposits is a complex function of igneous source, magmatic crystallization, hydrothermal modification, and supergene enrichment during weathering (Bern et al., 2017; Hei Martin Li et al., 2017; Smith et al., 2016; Xu et al., 2017). One of the major consequences of the redistribution process in weathering profiles developed on granito-gneissic rocks is the accumulation of exchangeable REY, leading to the most important REY ores, namely "easily worked deposits," especially in China for HREE (Bao & Zhao, 2008; Simandl, 2014; Smith et al., 2016; Xu et al., 2017). Thus, finding models of how hydrothermal alteration and chemical weathering influence the accumulation of REY ion-adsorption on granito-gneissic rocks is also an important topic of research (Bern et al., 2017).

In a companion paper (Braun et al., 2017), we explored the combined influence of chemical weathering (i.e., from heavy accessory bearing minerals breakdown), atmospheric dusts leaching and vegetation cycling on the solute dynamics of REY-Th-U in the extensively studied tropical forested Mule Hole CZO, South India. We showed that REE and Th, mainly from atmospheric dust leaching origin, are significantly recycled by vegetation and exported by overland flow as organic complexes in the ephemeral stream while solute export by groundwater is much more significant for U than for REE and Th.

In the present paper, we study the mobilization of REY-Th-U from the breakdown of accessory REY-Th-U bearing primary and authigenic minerals, their fractionation, redistribution, and transfer in the granito-gneiss-regolith-sediment system in order to clarify the source to sink behavior of REY-Th-U and to highlight the link between the successive processes. The elemental sources were inferred from the geochemistry and mineralogy of the parent gneiss, weathering profiles (ferralsol and vertisol), and streambed and suspended sediments, with special emphasis to hydrothermal alteration prior to the onset of weathering. Moreover, batch leaching experiments of the parent gneiss and extractions of cation-exchangeable and iron-related pools of soils were also carried out to infer the potential initial and secondary REY-Th-U sources reactive to weathering processes.

2. Settings

The Mule Hole CZO was established in 2003 as part of the Environmental Observatory BVET (Figure 1, https://mtropics.obs-mip.fr/experimental-tropical-watersheds-2/) by the French "Drainage Basins Network" (Réseau des Bassins Versants, RBV; http://rnbv.ipgp.fr/) and the "Infrastructure de Recherche" OZCAR (Observatoire de la Zone Critique: Applications et Recherches). This 4.10 km^2 watershed is located 11°72′N and 76°42′E in the subhumid part of the climatic gradient of the Kabini river basin in the Southwest part of Peninsular India.

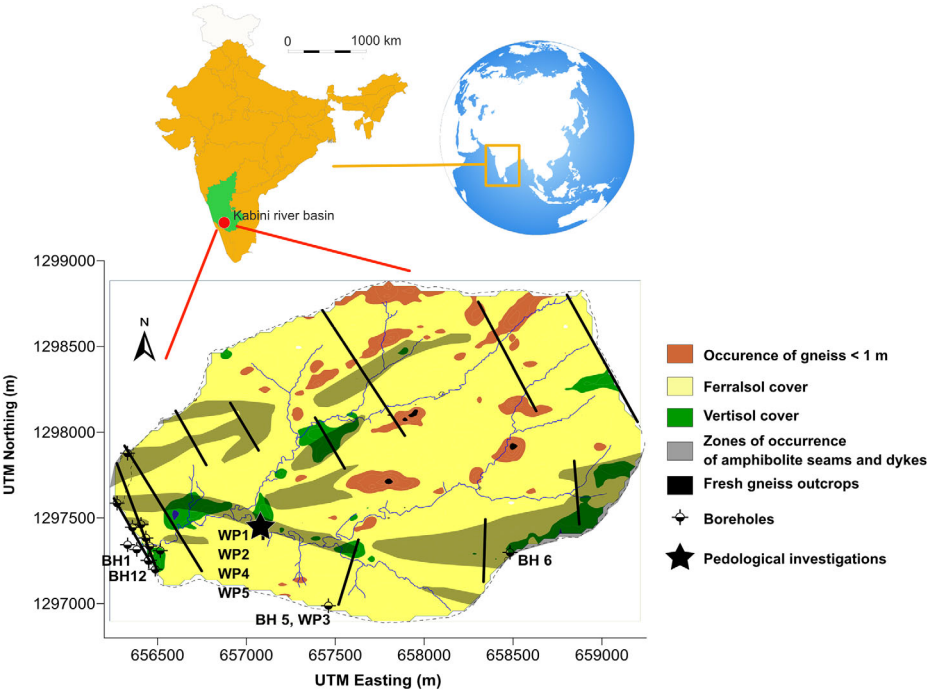


Figure 1. Location of sampling sites (boreholes, BH; soil pits, WP) and regolith features of the Mule Hole watershed (adapted from Braun et al. [2009]).

The regolith architecture and composition have been thoroughly investigated (Braun et al., 2009; Maréchal et al., 2009, 2011; Riotte et al., 2014a, 2014b, 2018; Ruiz et al., 2010; Violette et al., 2010a). The parent rocks consist of Peninsular gneiss of the >2.8 Ga West Dharwar craton (Naqvi & Rogers, 1987) mainly composed of quartz and Na-plagioclase as major minerals and amphibole, sericite, biotite, and epidote as minor minerals. The gneiss exhibits pronounced hydrothermal alteration features, as illustrated by numerous hydrothermal seams rich in calcite, epidote and albite. The alteration of the major phases is characterized by sericitization of plagioclase and chloritization of biotite by the pervasive fluids. Epidote is widespread. The dominant parent gneiss is intermingled with much less abundant mafic to ultramafic rocks, mostly amphibolite (Shadakshara Swamy et al., 1995). The amphibolite is composed of hornblende and anorthite as major mineral and calcite, epidote, as minor minerals. At the watershed scale, the gneissic rocks cover 85% of the whole area against 15% for the mafic to ultramafic rocks.

The saprolite has developed downward at the expense of the underlying fractured gneissic parent rock from which it does retain the structure and the fabric (i.e., isovolumetric weathering). The saprolite is immature and still contains significant amount of unweathered primary minerals like plagioclase. At the watershed scale, the average regolith thickness is 17 m (Braun et al., 2009) of which 2 meters of soil cover is present, on average. The latter is composed of (i) ferralsols on the hill slopes (66% of the whole watershed area), (ii) vertisols either on flat valley bottoms on undifferentiated bedrocks and in the depressions on the crest line on amphibolite-rich bedrock (12% of the whole watershed area), and (iii) saprolite outcrop topped by thin ferralsol layers (22% of the whole watershed area) (Barbiéro et al., 2007). The soil cover develops at the expense of either saprolite (e.g., ferralsol) or colluviums/alluviums (e.g., vertisol) at the uppermost part of the regolith where the perturbation brought by both physical and biological processes lead to (i) the differentiation into horizons and (ii) the loss of the existing isovolumetric weathering features of the underlying saprolite. The ferralsol cover depth varies from 1 to 2 m on the hill slopes while the vertisol cover average depth is of 2 m on the lower part of the hill slopes and flat valley bottoms. Thicker black soils (2.5 m) are also developed on amphibolite-rich bedrock located in the depressions on the crest line. An assemblage of secondary clays and clay minerals dominated by kaolinite and goethite characterizes the ferralsol mineralogy. Residual crystals of quartz, sericite, and, to a lesser extent, Na-plagioclase, are preserved till the topsoil. The mineralogy of the gneiss-derived vertisols is dominated by smectite in the secondary

clay assemblage upon kaolinite and kaolinite-smectite interstratified. In the amphibolite-derived vertisol, the mineralogy is dominated by smectite. The vertisol matrix contains pedogenic carbonates either disseminated tiny or as pluricentimetric botryoidal nodules witnesses of past dryer climatic conditions (Violette et al., 2010b).

3. Materials and Methods

3.1. Sampling

The gneissic parent rock was collected either as cuttings in the borehole network or as blocks on outcrops. The borehole samples (BH1, BH5, BH12) represent a composite sampling of the gneiss at the CZO scale (Braun et al., 2009) including both leucratic and melanocratic zones. The dynamiting carried out next to the outlet of the Mule Hole CZO (Soreda Halla bridge) enabled the collection of fresh samples of leucocratic gneiss (GNMH) and crosscutting epidote-rich hydrothermal seams (GNENC). A melanocratic gneiss sample (GNJJ) was also collected in a rivulet bed (Figure 1). The amphibolite samples correspond to the cuttings collected from the BH6 borehole.

The gneiss saprolite samples were selected from BH1, BH12, and BH5 after chemical identification with weathering indices (see procedure in Braun et al. [2009]). Three profiles of ferralsol (WP1, WP2, WP3) and two of vertisol (WP4, WP5) were sampled. WP3 corresponds to the top part of the borehole BH5 at the ridge-top and represents the top of a saprolite truncated by erosion, on which pedogenic processes have led to the formation of a thin ferralsol. The other soil profiles belong to the T1 soil catena, close to the stream (Barbiéro et al., 2007). The down slope profiles WP1 (ferralsol) and WP5 (vertisol) represent more evolved, deeper soils developed on saprolite (estimated at a depth of about 5–6 m), wherein the topmost part (up to about 120–150 cm) is composed of proximal colluvial material fed by less weathered upslope zones and/or biological activity of termites (Jouquet et al., 2016a, 2016b, 2016c).

About 10 kg of streambed sediment samples were collected (i) at the outlet of the Mule Hole brook and (ii) in three other streambeds draining neighboring areas. The streambed sediment samples were sieved to collect the fine sand size fraction (100–200 μm) for heavy liquid separation subsequently. The sandy streambed sediment can be considered as a watershed integrative for the residual minerals from the erosion of the soil cover.

Composite samples of suspended sediments from three floods of the year 2005 were collected by filtration through 0.22 μm Sartorius® cellulose acetate membranes at the outlet of the Mule Hole CZO. About 100 mg of each were collected for bulk analysis.

3.2. Bulk Geochemical Analyses and Density Measurements

The analyses of REY-Th-U and selected elements (Zr, Ti, P, Fe, Ca, Na) from bulk parent rock samples (BH1, BH5, BH12, BH6, GNJJ, GNMH, GNENC), saprolite (BH1, BH5, BH12), soils (WP1 to 5) and streambed and suspended sediments were performed with ICPMS after $LiBO_2$ fusion and HNO_3 dissolution at SARM Nancy (Centre de Recherches Pétrographiques et Géochimiques-CNRS, Vandœuvre-lès-Nancy). Detection limits and uncertainties are presented in supporting information Data sets S1 (Carignan et al., 2001).

The bulk and grain soil density measurements were performed at the Indo-French Cell for Water Sciences (IFCWS, Bangalore, India) with a Sartorius® density kit on a sample set of ten aggregates and on aliquots crushed and dried at 105°C for 24 h using a pycnometer, respectively. The $CaCO_3$ contents of bulk soil samples (WP1, WP5) and the grain size distribution were determined at the Laboratory of Soil Analyses, Arras, France (LAS, INRA, https://www6.npc.inra.fr/las/).

3.3. Mass Balance Calculation

The mass balance equation set is based on the principle of mass conservation (Brimhall et al., 1991; Oh & Richter, 2005). For a chemical element *j*:

$$\frac{V_w \rho_w C_{j,w}}{100} = \frac{V_p \rho_p C_{j,p}}{100} + m_{j,flux}$$

Where the subscripts *p* and *w* refer to the parent and weathered materials, respectively. *V* is volume in cm^3, ρ is bulk density in g/cm^3, and C_j is chemical concentration of any element *j* in weight percent (wt%). The

$m_{j,flux}$ represents the mass of an element j moving in or out of the system. The $m_{j,flux}$ is positive if the element j is accumulated in the system and negative if j is leached from the system. The volumetric strain (ε) or volume change is calculated from the density ratios ρ and conservative element concentrations C_j in the regolith by:

$$\varepsilon_{i,w} = \frac{\rho_p C_{i,p}}{\rho_w C_{i,w}} - 1$$

Positive values of $\varepsilon_{i,w}$ indicate expansion, negative values indicate collapse and values around zero, isovolumic weathering.

The addition or subtraction of a chemical element j, either by solute migration or mechanical translocation, is quantified by the open-system mass fraction transport function ($\tau_{j,w}$):

$$\tau_{j,w} = \left(\frac{\rho_w C_{j,w}}{\rho_p C_{j,p}}\right) \cdot \left(\varepsilon_{i,w} + 1\right) - 1$$

Because the calculation of $\tau_{j,w}$ takes into account both residual enrichment and deformation, a positive value for $\tau_{j,w}$ reflects a true mass gain in element j of the weathered rock compared to the parent rock and a negative value indicates a mass loss. If $\tau_{j,w} = 0$, the element is immobile during weathering with respect to the volume of regolith considered.

The mass balance equations were applied in selected profiles for ferralsol (WP1, WP3) and vertisol (WP5) developed on gneiss and saprolite from BH1, BH5 and BH12 (from 4 to 20 m depth). Ti was used as inert element in the calculations (see explanations in Braun et al. [2009] and Violette et al. [2010b]). The elemental behavior is sorted out according to their mass transfer profiles: immobile, depletion, depletion-enrichment, addition, and biogenic profiles (Brantley & Lebedeva, 2011).

3.4. Batch Leaching Experiments of Parent Gneiss: Extraction of Cation-Exchangeable and Iron-Related Pools of Soils

Two leaching experiments were carried out to identify the REY-Th-U sources from the gneiss-forming minerals and from the soil types, according to the selected grain size fractions.

The first experiment was an acid leaching batch experiment carried out with the leucocratic gneiss GNMH for 8 weeks according to the methodology of Erel et al. (2004). Four aliquots of 2 g of GNMH gneiss powder, namely GN1, GN2, GN3, and GN4, were mixed each with 400 mL of HNO_3 0.1 *N* (solid/liquid ratio of 1/200) in pre-cleaned 500 mL Savillex® digestion beakers. The vessels were constantly stirred at 230 rpm at 25°C in a rotate shaker. After 1 week, all the vessels were removed from the stirrer, kept in a clean room over night with loosened lids to allow settling the gneiss powder and equilibrating the acid leachate with atmosphere. Then the leachate was collected with syringe and was filtered using 0.2 μm acetate cellulose filters. Solutions were stored in precleaned polypropylene bottles for further multielement analyses by ICP-MS (GET, Toulouse). Except for GN1, the vessels were refilled with 400 mL of a new 0.1 *N* acid solution. For the other vessels, the procedure was applied so on and so forth at fixed day and time: Three times for GN2 (weeks 1 to 3), 6 times for GN3 (weeks 1 to 6), and 8 times for GN4 (weeks 1 to 8). The stability of the pH in the leachate was checked regularly. At the end of the leaching experiments, the remaining powder was dried up prior to XRD analysis. The weighing of the containers at each step of the procedure allowed assessing the loss of matter during the filtration and sampling steps.

The second experiment consisted in four extractions on ferralsol (profile WP1) and vertisol (profile WP5) samples collected at 100–120 cm depth. These samples are representative of the material that can be removed by erosion. Due to the experimental nature of extractions, the results indicate only trends of the potential leaching in natural regolith system where a continuum in the leachable phases exists (Ma et al., 2011). The extractions were performed on bulk soil and three grain size fractions (sand: 200–500 μm; silt + clay: <50 μm; clay: <1 μm). The first extraction was performed with ammonium acetate (NH_4OAc) 1 *M* (AFNOR NFX 31–108 norm), a usual procedure to recover the soil cation-exchangeable pool easily available for plant uptake or for leaching by drainage. An aliquot of 2.5 g of powdered soil is stirred in 50 mL of ammonium acetate (NH_4OAc) 1 *M* at 25°C for 20 min.

The second and third acid extractions aimed at recovering elements potentially adsorbed or included in the secondary Fe-Mn oxides and hydroxides phases that accumulate during soil genesis. As we focus on trace elements, we adapted the protocol used for iron isotopes fractionation in weathering studies (Buss et al., 2010; Chapman et al., 2009; Guelke et al., 2010; Wiederhold et al., 2007). The second extraction was carried out with HCl 0.5 *M* in which the soil sample powders were stirred at 25°C for 24 h with liquid to solid ratio being 25. It enabled to dissolve exchangeable, adsorbed, organic-bound, and poorly crystalline Fe oxides and oxyhydroxides. HCl-soluble minerals, such as carbonates and phosphates, might also be sensitive to this treatment. However, in sequential extraction of phosphorus pools in soils, the dissolution of phosphate minerals is usually achieved with a stronger acid, for example, HCl 1 *M* (Cross & Schlesinger, 1995; Hedley et al., 1982). The third extraction was carried out with HCl 5 *M*. The soil powders were stirred at 25°C for 24 h with liquid to solid ratio of 25 again. Usually, HCl 6 *M* is used in iron isotopes studies as it achieves a complete dissolution of all crystalline iron oxide minerals such as goethite and hematite (Schwertmann & Pfab, 1996). But this acid molarity is already too strong to prevent the partial dissolution of sensitive minerals as phyllosilicates.

3.5. Mineralogical Investigations and Analyses

The parent rock mineralogy and crystal chemistry were investigated in gneiss samples and in the Mule Hole streambed sediment either on thin sections or resin mounted mineral separates. The REY-Th-U soil mineralogy was only investigated on two ferralsol thin sections at two depths (100–120 and 300–320 cm). The samples from the shallow depth correspond to the samples which were leached in the extraction experiments.

The accessory and secondary minerals were systematically sought with Scanning Electron Microscopy (SEM Jeol JSM 6360LV) in backscattered electron (BSE) mode coupled to an EDS analysis system "Silicon Drift Detector" (SDS) PGT Sahara, at GET, Toulouse, France.

The chemical composition of some high content REY-Th-U bearing minerals was analyzed either by electron microprobe analyzer (EPMA) with CAMECA SX50 (allanite, bastnesite) at Geoscience Environnement Toulouse (GET, Toulouse) or with a CAMECA SX100 (monazite, xenotime, thorite) at the National Centre of Excellence in Geoscience Research-Geological Survey of India (NCEGR-GSI), Bangalore.

The in situ trace element analyses were carried out on thin sections (GNMH and GNJJ) and mineral separates mounted in resin (GNMH and streambed sediments) at the Géosciences Montpellier Laboratory (University of Montpellier) using a ThermoFinnigan ELEMENT XR high resolution (HR) ICP-MS, coupled with a Geolas (Microlas) automated platform housing a 193 nm Compex 102 laser from LambdaPhysik. Ablation experiments were conducted in an ablation cell of $\sim$30 cm^3 in a He atmosphere, which enhances sensitivity and reduces inter-element fractionation (Günther & Heinrich, 1999). The helium gas and particles from the sample were then mixed with Ar before entering the plasma. Data were acquired in the fast E-scan mode at low resolution ($M/\Delta M = 300$), devoting 2 min for the blank and 1 min for measurement of the analytes. The laser was fired using an energy density of 10 J/cm^2 at a frequency of 5 Hz and using a spot size between 26 and 102 μm depending on the mineral content in REY-Th-U. Oxide level, measured using the ThO/Th ratio, was below 0.8%. Depending on the minerals analyzed, ^{29}Si or ^{43}Ca was used as an internal standard and analyte concentrations were calibrated against the NIST612 reference material, using the values given in Pearce et al. (1997). Data were subsequently reduced using the GLITTER software (Van Achterberg et al., 2001) by carefully inspecting the time-resolved analysis to check for lack of heterogeneities (inclusions or fractures) in the analyzed volume.

4. Results

Table 1 displays the standard statistics for the contents of REY, Th, U, and selected elements (Zr, Ti, Fe, Ca, Na, P) for parent rocks (gneiss and amphibolite), regolith (saprolite, ferralsol, vertisol) and streambed and suspended sediments. The sums of Light Rare Earth Elements (LREE), Heavy Rare Earth Elements (HREE) and Rare Earth Elements + yttrium (REY), the Upper Continental Crust (UCC) normalized ratios and anomalies are indicated. The full data set is reported in supporting information Data sets S2 and S3 including, for the soil cover, the measured bulk and grain densities and Chemical Index of Alteration.

Geochemistry, Geophysics, Geosystems

10.1029/2018GC007453

Table 1

Standard Statistics for the Contents of REY-Th-U and Selected Elements (Zr, Ti, Fe, Ca, Na, and P) for (i) the Parent Rocks (Gneiss and Amphibolite), (ii) the Regolith Developed on Gneiss (Saprolite, Ferralsol, and Vertisol), and (iii) the Exported Streambed and Suspended Sediments[a]

		La (μg/g)	Ce (μg/g)	Pr (μg/g)	Nd (μg/g)	Sm (μg/g)	Eu (μg/g)	Gd (μg/g)	Tb (μg/g)	Dy (μg/g)	Ho (μg/g)	Er (μg/g)	Tm (μg/g)	Yb (μg/g)	Lu (μg/g)	Y (μg/g)	Th (μg/g)	U (μg/g)	Zr (μg/g)	Ti (μg/g)	Fe (μg/g)	Ca (μg/g)	Na (μg/g)	P (μg/g)	CIA	∑LREE (μg/g)	∑HREE (μg/g)	∑REY (μg/g)	$(LREE/HREE)_N$	La/Sm_N	Gd/Yb_N	Ce/Ce*	Eu/Eu*
GNEISSIC	Average	38.24	72.77	8.21	30.41	6.02	1.44	5.36	0.80	4.58	0.88	2.42	0.35	2.32	0.36	23.85	8.52	0.78	169	2,179	29,079	16,005	34,866	401	52	157	17	198	1.46	1.19	1.33	0.97	1.36
ROCK,	Median	30.01	56.25	6.07	22.02	4.47	1.08	3.51	0.49	2.68	0.51	1.44	0.21	1.42	0.22	14.44	7.08	0.58	139	2,128	26,523	11,900	36,173	384	53	120	10	162	1.42	1.13	1.24	0.98	1.23
n = 41	±σ	26.80	49.74	5.66	22.40	5.11	0.89	4.96	0.77	4.50	0.88	2.47	0.37	2.47	0.38	22.93	6.24	0.53	84	939	15,344	19,491	8,471	133	3.6	106	16	126	0.99	0.63	0.46	0.04	0.75
	Min	11.86	21.47	2.30	7.87	1.30	0.56	0.96	0.12	0.57	0.09	0.25	0.03	0.22	0.04	2.54	1.00	0.15	61	581	11,149	3,345	13,146	140	43	47	2	52	0.22	0.26	0.58	0.86	0.75
	Max	142.40	232.00	27.37	110.10	23.88	5.05	25.11	4.04	23.88	4.73	13.42	2.03	13.93	2.14	124.00	32.01	2.45	405	5,095	79,212	123,449	49,156	768	60	505	89	601	5.00	2.97	2.56	1.05	5.37
AMPHIBOLITE,	Average	3.77	9.94	1.50	7.64	2.66	1.05	3.61	0.65	4.35	0.91	2.60	0.39	2.58	0.39	25.50	0.40	0.10	70	6,960	102,627	61,989	18,599	1,171	41	27	15	68	0.18	0.21	0.69	0.98	1.47
n = 24	Median	3.69	9.85	1.45	7.41	2.70	1.07	3.78	0.68	4.53	0.94	2.65	0.40	2.63	0.40	26.55	0.38	0.10	75	7,315	106,802	61,567	17,701	1,180	40	26	16	69	0.19	0.21	0.68	0.99	1.44
	±σ	0.81	2.22	0.32	1.54	0.47	0.17	0.66	0.12	0.79	0.16	0.47	0.07	0.48	0.07	4.79	0.16	0.03	16	1,627	16,543	10,763	3,914	410	3.3	5	3	12	0.02	0.01	0.04	0.03	0.08
	Min	2.35	6.53	0.99	5.18	1.77	0.71	2.30	0.42	2.80	0.59	1.65	0.24	1.60	0.25	16.46	0.17	0.05	36	4,423	72,945	40,995	9,778	630	36	18	10	44	0.14	0.19	0.63	0.91	1.36
	Max	5.47	14.56	2.19	10.96	3.59	1.39	4.74	0.85	5.58	1.19	3.44	0.52	3.49	0.53	34.15	0.82	0.15	96	10,015	142,533	76,458	26,677	2,620	47	38	20	93	0.21	0.25	0.76	1.03	1.66
SAPROLITE,	Average	33.27	68.17	7.97	31.16	6.61	1.64	6.09	0.94	5.60	1.10	3.13	0.46	3.08	0.47	30.94	6.93	0.88	223	2,092	24,376	10,778	31,027	304	57	149	21	201	1.46	1.08	1.32	1.01	1.29
n = 20	Median	31.72	65.40	6.78	23.65	3.88	1.03	2.69	0.36	1.87	0.35	0.97	0.14	0.95	0.15	10.18	6.01	0.69	147	1,975	23,911	11,792	26,863	275	56	137	7	158	1.80	1.21	1.36	0.97	1.31
	±σ	10.29	24.16	3.90	19.10	5.63	1.23	6.16	1.03	6.52	1.34	3.90	0.58	3.98	0.61	36.86	3.09	0.66	163	726	9,604	7,427	7,757	129	4.9	61	24	115	0.81	0.48	*0.36*	*0.18*	*0.23*
	Min	14.46	25.83	3.25	12.31	2.54	0.64	1.75	0.23	1.13	0.19	0.52	0.07	0.48	0.07	5.80	1.98	0.37	103	1,019	9,072	1,051	19,229	140	49	59	4	79	0.29	0.36	0.49	0.85	0.92
	Max	58.17	123.80	17.93	79.35	19.98	4.59	19.97	3.10	18.37	3.94	12.25	1.93	13.41	2.07	110.10	14.92	2.87	661	3,662	41,911	26,079	46,863	554	66	304	67	468	2.72	1.75	1.89	1.73	1.606
FERRALSOL,	Average	27.34	54.09	6.15	23.30	4.63	1.03	4.15	0.63	3.72	0.73	2.12	0.32	2.21	0.35	21.06	9.37	1.23	290	2,912	39,479	3,642	5,674	146	81	117	14	152	0.86	0.88	0.91	1.19	1.02
n = 33	Median	27.96	52.50	6.25	23.65	4.67	1.06	4.20	0.64	3.86	0.76	2.19	0.33	2.24	0.35	21.83	8.26	1.34	279	3,027	37,763	4,210	4,199	135	82	114	15	152	0.82	0.91	0.92	0.93	1.04
	±σ	10.74	19.16	2.30	8.76	1.63	0.36	1.34	0.19	1.02	0.19	0.54	0.08	0.54	0.09	5.82	4.49	0.42	115	821	9,478	1,271	4,374	35	4.9	35	4	43	0.13	0.13	0.15	0.84	0.08
	Min	3.00	30.34	0.75	2.77	0.76	0.13	0.98	0.19	1.34	0.28	0.81	0.13	0.95	0.15	8.13	3.87	0.54	77	713	10,674	1,394	1,528	83	64	38	5	54	0.68	0.60	0.36	0.32	0.67
	Max	53.82	123.40	11.56	44.38	8.40	1.90	7.09	1.02	5.78	1.12	3.16	0.48	3.20	0.52	34.44	26.98	2.21	724	3,962	59,110	5,346	24,696	227	90	190	22	236	1.21	1.13	1.17	4.77	1.10
VERTISOL,	Average	22.64	42.58	4.99	18.80	3.78	0.96	3.30	0.51	3.02	0.60	1.69	0.26	1.74	0.27	17.03	8.10	1.13	203	2,980	29,327	10,846	13,162	120	67	94	11	122	0.97	0.92	1.06	0.94	1.17
n = 15	Median	22.85	40.45	5.08	19.17	3.92	1.01	3.44	0.55	3.22	0.63	1.80	0.27	1.84	0.29	17.98	6.80	1.11	196	3,075	31,916	10,249	10,668	120	69	94	12	124	0.82	0.89	0.92	0.91	1.18
	±σ	2.69	10.52	0.59	2.31	0.55	0.18	0.61	0.12	0.75	0.16	0.45	0.07	0.46	0.07	5.16	4.77	0.15	37	410	8,314	3,064	7,803	21	5.9	15	3	19	0.57	0.15	0.58	0.18	0.08
	Min	17.96	35.30	3.99	14.90	2.62	0.43	1.60	0.16	0.66	0.10	0.24	0.03	0.25	0.05	0.25	5.11	0.94	130	2,224	5,631	7,583	9,755	79	51	76	3	92	0.76	0.83	0.86	0.80	0.92
	Max	26.28	78.80	5.76	21.78	4.42	1.13	3.89	0.62	3.67	0.73	2.06	0.32	2.10	0.33	21.67	24.73	1.51	271	3,464	38,392	20,905	41,106	161	71	137	14	171	3.03	1.46	3.14	1.54	1.25
STREAM	Average	5.36	11.18	1.08	3.85	0.76	0.19	0.65	0.10	0.58	0.12	0.34	0.05	0.38	0.06	3.30	1.30	0.26	116	641	8,309	3,625	7,072	<DL	52	22	2	28	1.12	1.09	1.47	1.09	1.18
SEDIMENTS,	Median	5.54	11.33	1.13	4.04	0.72	0.17	0.61	0.09	0.60	0.13	0.38	0.06	0.41	0.07	3.52	1.09	0.25	88	435	8,306	3,291	6,769		52	23	2	30	0.92	1.11	1.52	1.07	1.17
n = 4	±σ	0.97	2.26	0.15	0.52	0.13	0.06	0.15	0.03	0.16	0.04	0.10	0.02	0.12	0.02	0.99	0.49	0.06	77	454	2,485	936	2,508		0.9	4	1	4	0.47	0.24	0.33	0.08	0.12
	Min	4.14	8.29	0.86	3.09	0.64	0.15	0.52	0.07	0.38	0.07	0.20	0.03	0.22	0.04	1.98	0.98	0.21	58	378	5,379	2,930	4,681		51	17	2	23	0.83	0.81	1.04	1.03	1.06
	Max	6.21	13.79	1.17	4.22	0.95	0.28	0.87	0.13	0.76	0.16	0.42	0.07	0.49	0.09	4.21	2.03	0.34	230	1,319	11,247	4,989	10,067		53	26	3	30	1.81	1.33	1.81	1.21	1.33
STREAM	Average	24.57	47.91	5.39	20.04	4.13	1.07	3.62	0.57	3.51	0.72	1.94	0.28	1.88	0.28	18.96	7.48	1.37	123	3,900	49,737	10,520	7,107	<DL	75	103	13	135	0.86	0.90	1.11	0.98	1.20
SEDIMENTS,	Median	24.71	49.27	5.38	20.06	4.09	1.04	3.53	0.55	3.41	0.71	1.92	0.28	1.87	0.28	18.53	7.62	1.33	123	3,842	49,038	10,227	6,758		75	105	13	135	0.85	0.90	1.10	0.97	1.21
n = 3	±σ	1.30	2.74	0.24	1.05	0.21	0.07	0.17	0.03	0.18	0.04	0.09	0.02	0.10	0.01	1.04	0.30	0.17	19	167	2,610	809	663		0.2	5	1	7	0.04	0.01	0.03	0.02	0.02
	Min	23.21	44.76	5.16	18.98	3.95	1.03	3.52	0.55	3.40	0.69	1.87	0.27	1.79	0.27	18.21	7.13	1.22	105	3,770	47,548	9,898	6,692		75	97	12	128	0.83	0.89	1.09	0.96	1.18
	Max	25.79	49.69	5.63	21.09	4.36	1.15	3.82	0.60	3.72	0.76	2.04	0.30	1.99	0.30	20.15	7.67	1.56	143	4,088	52,626	11,435	7,871		75	108	14	141	0.90	0.92	1.15	1.01	1.22

[a]The Chemical Index of Alteration (CIA) are also indicated. The REY-Th-U contents are normalized to the contents of the Upper Continental Crust (UCC) (Rudnick & Gao, 2003) and used to calculate the following normalized ratios and anomalies: $(LREE/HREE)_N = \left(\sum LREE_{sample}/\sum LREE_{UCC}\right) / \left(\sum HREE_{sample}/\sum HREE_{UCC}\right)$ $(La/Sm)_N = \left(La_{sample}/La_{UCC}\right)/\left(Sm_{sample}/Sm_{UCC}\right)$ $(Gd/Yb)_N = \left(Gd_{sample}/Gd_{UCC}\right)/\left(Yb_{sample}/Yb_{UCC}\right)$ $Ce/Ce^* = \left(Ce_{sample}/Ce_{UCC}\right)/\left(La_{sample}/La_{UCC}\right)^{0.5} \times \left(Pr_{sample}/Pr_{UCC}\right)^{0.5}$ $Eu/Eu^* = \left(Eu_{sample}/Eu_{UCC}\right)/\left(Nd_{sample}/Nd_{UCC}\right)^{0.5} \times \left(Gd_{sample}/Gd_{UCC}\right)^{0.5}$

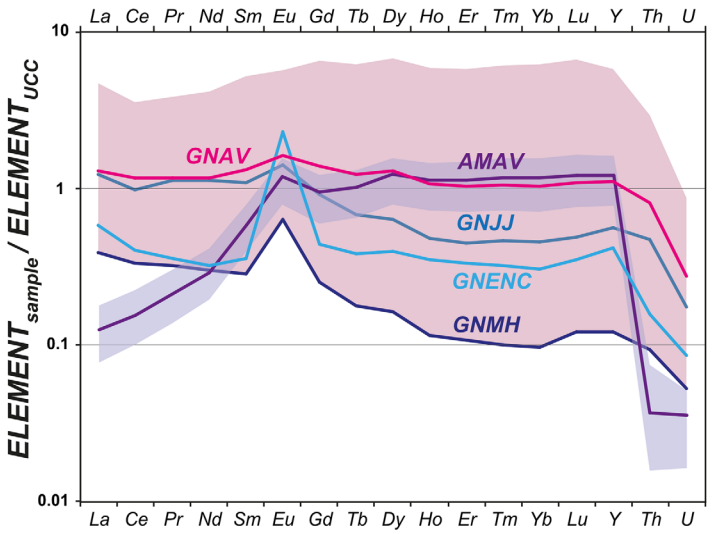


Figure 2. UCC-normalized REY-Th-U patterns for average gneiss (GNAV) and average amphibolite (AMAV). The rose and purple shaded areas represent the envelope of REY-Th-U contents. The patterns for the leucocratic gneiss end-member (GNMH), hydrothermalized enclave (GNENC), and melanocratic gneiss (GNJJ) are also indicated.

4.1. Parent Rocks

4.1.1. Gneiss and Amphibolite Whole Rock Composition

In the gneiss, average REY contents are of 200 μg/g (80% of LREE), 0.8 μg/g of U, 8.7 μg/g of Th, 170 μg/g of Zr, 2,200 μg/g of Ti, and 400 μg/g of P (Table 1). Overall, some good positive inter-correlations ($r^2 \geq 0.8$) exist between Th, Zr, LREE, and U. The inter-correlations decline with HREY, P, and Ti ($r^2 \leq 0.6$). The UCC-normalized patterns of gneiss show a large variability (Figure 2). The average pattern (GNAV) displays a slight enrichment in LREE (LREE/HREE$_N$ = 1.5) and a significant depletion in U. There is no Ce-anomaly (Ce/Ce* = 1) and Eu-anomaly (Eu/Eu*) ranges from 0.8 to 5.8. The leucocratic end-member of gneiss (GNMH) and the hydrothermal seam (GNENC) have the lowest REY contents (<80 μg/g) and the highest positive Eu anomaly, 3.5 and 5.8, respectively (Figure 2). The LREE, Th, U, and Zr contents of the average amphibolite are systematically lower than those of the average gneiss while the HREY contents are of the same order of magnitude (Table 1). The amphibolite UCC-normalized pattern displays a strong negative LREE fractionation (La/Sm$_N$ = 0.2), a slight HREE fractionation (Gd/Yb$_N$ = 0.8), a significant positive anomaly (Eu/Eu* = 1.6), and a strong depletion in both Th and U (Figure 2). The Ti and P contents are higher than those of gneiss with average of 7,000 and 1,200 μg/g, respectively. Taking into account the relative areas of amphibolite and gneiss at the watershed scale (0.15/0.85), the amphibolite accounts for only 6% of REY (3% of LREE, 16% of HREE, 19% of Y), 2% of U, 1% of Th, 7% of Zr but 56% of Ti and 54% of P.

4.1.2. Gneiss Mineralogy and Mineral Chemistry

The accessory phases observed in the parent gneiss are allanite [(LREE, Ca)$_2$(Al,Fe$^{III/II}$)$_3$(SiO$_4$)$_3$(OH)], bastnesite (LREECO$_3$F), titanite [(Ca,REE)(Ti,Fe^{III})SiO$_5$], pyrite (FeS$_2$), chalcopyrite (CuFeS$_2$), zircon [(Zr,Hf,HREE,Y,P)-SiO$_4$], and apatite [Ca$_5$(PO$_4$)$_3$(F,Cl,OH)]. Allanite appears as euhedral crystal invariably rimmed by epidote (Figure 3a). Most of the allanite crystals are altered and replaced, sometimes completely, by LREE-carbonate (bastnesite) and an alumino-silicate phase in the core zone (Figures 3a and 3b). The allanite crystals in GNMH are more affected by the replacement of bastnesite than in GNJJ. Titanite occurs as sub-euhedral crystal (Figure 3c) or, more commonly, as anhedral secondary inter-cleavage growth between biotite lattice along with epidote, Fe oxides and Fe-Ti oxides (Figures 3d and 3e). Zircon occurs as prismatic to rounded crystal which varies in size from 10 to 500 μm in length, the larger one displaying zoning (Figures 3f and 3h). Apatite crystals are euhedral to sub-euhedral, 50–500 μm wide without zoning (Figure 3g). They sometimes contain tiny zircon inclusions (Figure 3h). The hydrothermal seam (GNENC) is mainly composed of epidote, Na-plagioclase (albite), calcite and quartz. Albite is comparatively fresh. The identified accessory minerals are pyrite and anhedral allanite crystals as inclusions in epidote. The lighter grain size fraction of 100–200 μm (fine sand, d < 2.9 g/cm^3) from the Mule Hole streambed sediment (MHSS) is mainly composed of rounded quartz and highly weathered Na-plagioclase grains while the heavier fraction (d > 2.9 g/cm^3) contains subangular Fe-Ti oxides, amphibole, epidote, zircon, monazite [(LREE,Th)PO$_4$], and xenotime [(Y,HREE)PO$_4$] crystals. The monazite grains, more or less weathered with dissolution hollows, often contain xenotime, thorite (ThSiO$_4$), and thorianite (ThO$_2$) inclusions (Figures 4a–4d).

Table 2 lists the standard statistics for the composition of selected gneiss forming minerals in REY-Th-U. The dominant mineral reservoirs for LREE, HREE, Y, Th, and U content (content > 1,000 μg/g, Table 3) are in decreasing order: Monazite > allanite ≈ bastnesite > titanite ≈ xenotime ≈ thorite for LREE, xenotime ≈ thorite > monazite > titanite ≈ allanite > bastnesite for HREE and Y, thorite ≫ monazite > bastnesite ≫ xenotime for Th and thorite ≫ xenotime > monazite for U. The UCC-normalized patterns show a strong LREE enrichment in monazite, allanite, bastnesite, and Na-plagioclase (La/Sm$_N$ from 2.0 to 4.5) and a LREE depletion in epidote (0.2 < La/Sm$_N$ < 0.3), apatite (0.02 < La/Sm$_N$ < 0.12), titanite (La/Sm$_N$ = 0.05), and zircon (La/Sm$_N$ = 0.01) (Figure 5). The HREE fractionation is strongly positive in bastnesite (110 < Gd/Yb$_N$ < 410) and allanite (Gd/Yb$_N$ = 35), negative in epidote (0.1 < Gd/Yb$_N$ < 0.5) and in zircon

10.1029/2018GC007453

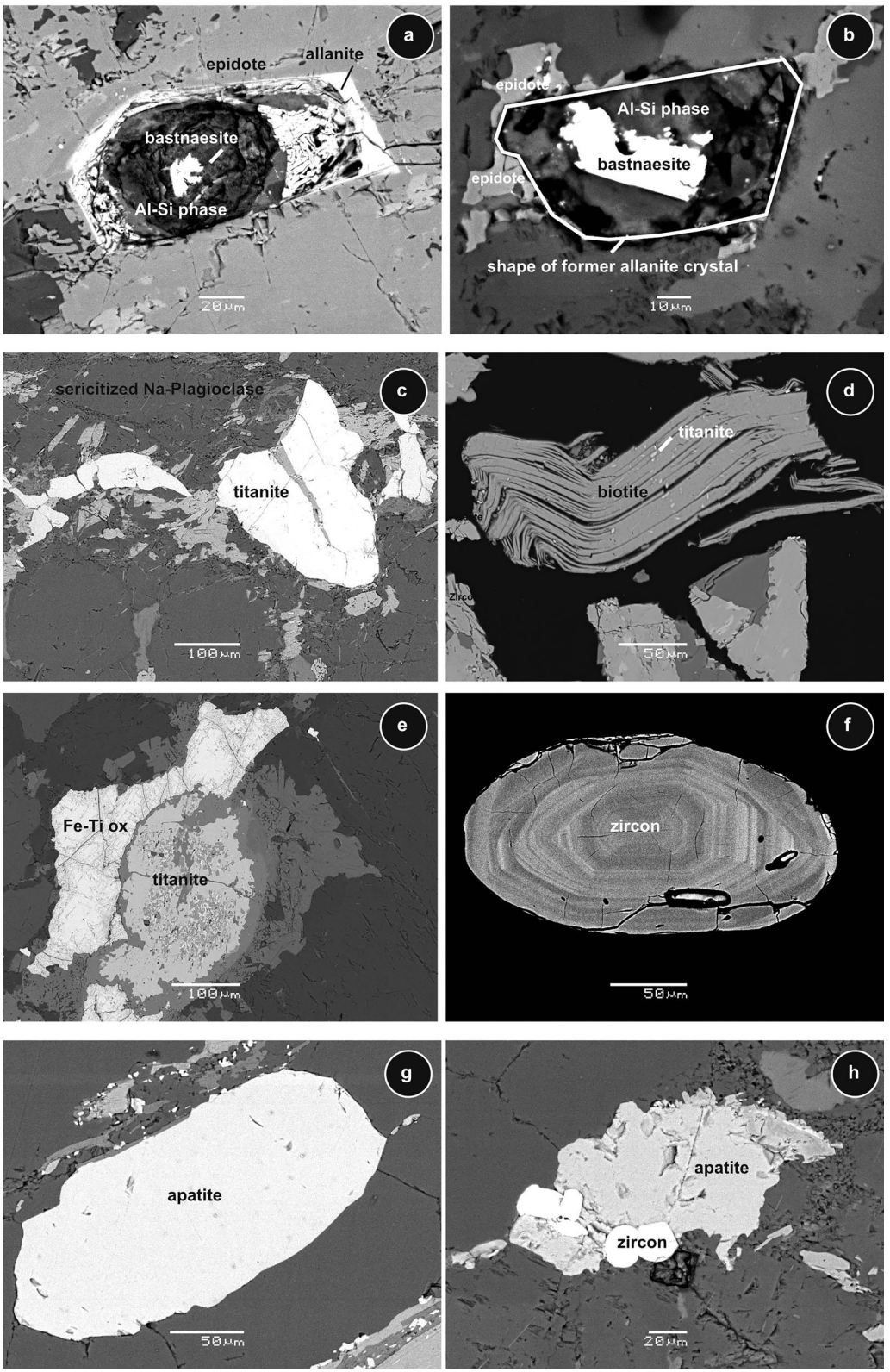


Figure 3. SEM-BSE images of REY-Th-U bearing minerals of the gneiss showing their petrographic relation in the rock. (a, b) Partially or completely altered allanite crystals replaced by bastnesite and alumino-silicate phases and rimmed by epidote crystals, (c) subhedral titanite crystal, (d) biotite having exsolution of titanite, (e) intergrowth of titanite with Fe-Ti oxides, (f) oscillatory zoned zircon, (g) large elliptical apatite crystal, and (h) apatite-zircon association.

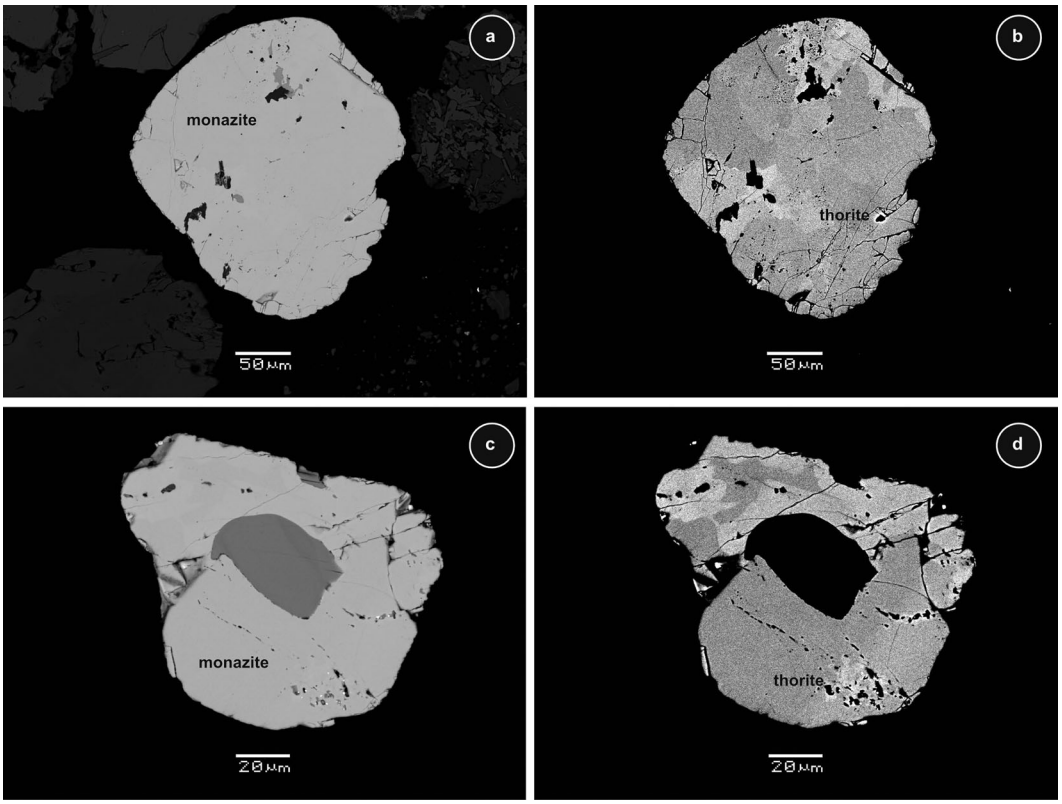


Figure 4. SEM-BSE microphotographs of rounded monazite crystals from stream sediments. (a, b) dissolution weathering features of monazite (same crystal, different BSE brightness), (c, d) thorite inclusions within monazite (same crystal, different BSE brightness).

($Gd/Yb_N = 0.03$), and not significant in apatite and titanite (Gd/Yb_N from 0.9 to 1.2). The Eu-anomaly is strongly negative in monazite, xenotime, zircon, allanite and bastnesite (Eu/Eu* from 0.1 to 0.5) and less significant in apatite and titanite with Eu/Eu* ranging from 0.8 to 1.3. The Eu-anomaly is positive in epidote and biotite with Eu/Eu* ranging from 4 to 8 and strongly positive in Na-plagioclase with Eu/Eu* of 28. Except the strong positive Ce-anomaly in zircon ($Ce/Ce^* = 19.6$), the other minerals do not show any Ce-anomaly.

4.1.3. Gneiss Leaching Experiments

The results of the batch leaching of the gneiss GNMH (leucocratic hydrothermalized end-member), free of resistant monazite and xenotime, are reported in supporting information Data set S4. Mimicking the chemical weathering of the main reactive REY-Th-U bearing mineral assemblage, i.e., allanite, bastnesite, and titanite as major ones and apatite and zircon as minor ones, the leaching experiments provide an overview of the leaching sequence. In terms of evolution in the leachate, the GNMH-normalized elemental ratios for HREE, LREE, U and Th (Figure 6a) show a huge increase at week 1 and then a progressive drop from weeks 2 to 8. In terms of the evolution of the GNMH-normalized specific ratios (Figure 6b), both Gd/Yb_N and La/Sm_N, initially of 2.6 and 1.5 for the Upper Crust normalized parent rock, show a progressive rise up to week 2 and then gently decrease until week 8. The Eu/Eu* anomaly, initially of 3.4 in the parent gneiss, shows a significant drop to 0.26 at week 2 followed by a slight increase up to 0.45 at week 8, while the Ce/Ce* anomaly remains stable around 1.

4.2. Composition of Gneiss-Derived Saprolite

The average contents (in µg/g) are of 191 for REY, 0.9 for U, 8.3 for Th, and 313 for P, respectively (Table 1). The UCC-normalized patterns (Figure 7) exhibit a large variability with significant ranges of Ce-anomalies ($0.9 < Ce/Ce^* < 1.7$), Eu-anomalies ($0.9 < Eu/Eu^* < 1.7$), La/Sm_N (0.4–1.8), and Gd/Yb_N (0.5–1.9). The range of the saprolite UCC-patterns is similar to those of parent gneiss.

Geochemistry, Geophysics, Geosystems

10.1029/2018GC007453

Table 2

Standard Statistics for the Contents of REY-Th-U and Selected Elements (Zr, Ti, Fe, Ca, Na, and P) for Selected Gneiss Forming Minerals Separated From Gneiss (GNMH, GNJJ) and Stream Sediments (MHSS)[a]

Mineral method, sample	Number of analyses		La (μg/g)	Ce (μg/g)	Pr (μg/g)	Nd (μg/g)	Sm (μg/g)	Eu (μg/g)	Gd (μg/g)	Tb (μg/g)	Dy (μg/g)	Ho (μg/g)	Er (μg/g)	Tm (μg/g)	Yb (μg/g)	Lu (μg/g)	Y (μg/g)	Th (μg/g)	U (μg/g)	∑LREE (μg/g)	∑HREE (μg/g)	∑REY (μg/g)	LREE/ $HREE_N$	Ce/ Ce*	Eu/ Eu*	La/ Sm_N	Gd/ Yb_N
Zircon (Zrn)																											
LA-ICPMS, thin section GNMH	7	Average	0.22	6.02	0.20	2.26	3.09	0.61	11.07	4.51	57.79	21.15	99.88	24.57	263.65	40.62	636.64	55.50	158.87	12.4	523.2	1,172.3	0.006	18.39	0.59	0.01	0.03
		±σ	0.33	1.70	0.21	1.86	2.29	0.20	8.05	3.29	40.27	13.65	60.10	14.14	147.21	22.26	399.15	45.18	88.58	4.8	302.8	702.3	0.010	15.39	0.20	0.01	0.03
		Min	0.03	2.84	0.04	0.60	1.32	0.35	4.36	1.00	8.16	2.33	10.09	2.40	26.52	4.21	71.32	17.11	55.64	6.6	59.6	147.5	0.002	1.65	0.29	0.00	0.01
		Max	0.93	8.40	0.65	5.18	7.89	0.91	27.77	10.96	131.97	44.02	190.46	43.51	433.58	62.67	1,274.07	142.57	320.88	20.6	941.5	2,236.1	0.029	37.06	0.97	0.04	0.11
Epidote (Epd)																											
LA-ICPMS, thin section GNMH	6	Average	17.37	39.56	6.43	33.72	11.32	14.14	10.13	1.94	12.44	2.42	7.34	1.22	10.46	1.58	70.86	0.26	2.84	122.5	47.5	240.9	0.20	0.89	8.16	0.29	0.64
		±σ	26.49	64.86	11.58	60.73	16.80	24.59	11.76	2.05	12.85	2.58	8.70	1.68	15.85	2.47	85.75	0.37	5.70	204.1	56.9	343.8	0.13	0.08	5.37	0.23	0.57
		Min	0.06	0.14	0.02	0.11	0.05	0.16	0.07	0.02	0.12	0.03	0.13	0.02	0.24	0.04	1.09	0.00	0.01	0.5	0.7	2.3	0.07	0.81	2.35	0.05	0.17
		Max	62.34	152.86	27.00	141.77	40.58	57.92	28.84	4.99	31.28	6.36	21.64	4.11	38.21	5.91	212.98	0.90	13.03	482.5	141.3	836.8	0.36	1.00	14.94	0.66	1.62
LA-ICPMS, thin section GNJJ	3	Average	1.85	2.05	0.65	2.96	1.14	3.35	1.18	0.26	2.80	0.74	4.24	1.07	9.42	1.23	24.76	0.15	0.19	12.0	20.9	57.7	0.08	0.45	16.45	0.24	0.09
		±σ	1.38	2.04	0.56	2.75	0.91	2.10	1.12	0.11	1.09	0.37	2.22	0.64	5.87	0.74	12.37	0.11	0.08	9.0	11.6	27.6	0.08	0.18	10.48	0.09	0.07
		Min	0.36	0.63	0.17	0.33	0.33	0.96	0.40	0.20	1.56	0.34	1.81	0.34	2.66	0.38	11.11	0.02	0.09	2.8	8.0	31.4	0.01	0.25	8.60	0.16	0.02
		Max	3.08	4.39	1.26	5.82	2.12	4.91	2.46	0.39	3.61	1.08	6.18	1.56	13.32	1.71	35.22	0.23	0.24	20.9	30.3	86.4	0.16	0.60	28.35	0.33	0.15
Na-plagioclase (Na-Plg)																											
LA-ICPMS , thin section GNMH	6	Average	5.90	8.25	0.71	2.69	0.53	3.26	0.90	0.08	0.47	0.10	0.38	0.03	0.23	0.04	3.30	0.36	0.09	21.3	2.2	26.9	1.94	0.98	28.49	2.05	ND
		±σ	5.05	6.21	0.56	2.11	0.39	2.40	0.53	0.08	0.43	0.10	0.31	0.04	0.23	0.03	2.55	0.53	0.09	16.2	1.6	19.6	2.44	0.10	17.04	1.17	ND
		Min	0.68	1.36	0.11	0.36	0.04	0.71	0.18	0.00	0.00	0.00	0.00	0.00	0.00	0.00	0.30	0.00	0.00	3.3	0.2	4.0	0.29	0.83	4.60	0.30	ND
		Max	13.95	16.57	1.50	5.54	1.01	6.61	1.41	0.19	1.10	0.25	0.65	0.09	0.52	0.08	6.49	1.32	0.19	43.5	4.0	52.7	6.86	1.14	56.73	3.60	ND
Biotite (Bi)																											
LA-ICPMS, thin section GNMH	9	Average	1.70	3.21	0.44	1.36	0.98	4.71	18.58	0.16	1.45	0.41	1.23	0.26	2.58	0.38	27.07	0.11	0.14	12.4	25.0	64.5	0.06	0.88	4.17	0.19	11.39
		±σ	1.07	1.36	0.19	1.06	0.46	5.31	17.52	0.14	1.02	0.31	1.12	0.32	2.76	0.40	17.04	0.15	0.21	6.0	14.6	35.8	0.02	0.17	3.33	0.09	17.87
		Min	0.34	0.79	0.25	0.00	0.00	0.96	4.39	0.00	0.00	0.00	0.00	0.00	0.00	0.00	13.25	0.00	0.00	4.0	12.8	30.1	0.03	0.62	2.11	0.08	0.33
		Max	3.92	4.77	0.87	3.24	1.45	16.51	57.81	0.39	3.40	0.90	3.06	0.87	7.79	1.10	66.49	0.45	0.58	22.0	59.5	144.7	0.10	1.12	11.54	0.36	52.85
Allanite (Aln),																											
LA-ICPMS, thin section GNMH	17	Average	44,668	92,272	9,430	32,571	3,486	268	3,635	153	375	44	156	8	48	5	1,009	731	170	187,935	4,425	193,370	4.38	1.00	0.37	2.15	46.04
EPMA, thin section GNMH	5	±σ	30,391	53,709	4,982	15,077	1,635	150	2,012	70	177	22	75	4	26	3	487	1,017	145	118,081	2,355	120,775	0.88	0.04	0.19	0.90	14.86
		Min	10,326	23,935	3,230	14,001	1,267	78	1,649	60	79	10	68	2	13	2	261	24	45	55,333	1,954	58,609	2.36	0.94	0.18	0.59	22.48
		Max	143,419	257,200	23,942	74,539	7,290	635	8,949	326	798	97	353	18	107	12	2,131	3,225	559	506,701	10,660	519,493	5.74	1.08	0.92	3.74	95.92
LA-ICPMS, thin section GNJJ	1	Average	30,573	65,940	7,500	29,502	2,929	239	594	49	171	22	50	4	25	3	602	275	45	17,793	919	19,314	2.03	0.99	1.50	0.49	13.82
EPMA, thin section GNJJ	10	±σ	7,321	15,832	2,751	7,782	1,207	ND	ND	ND	ND	ND	ND	ND	ND	ND	ND	ND	ND	ND	ND	ND	ND	0.14	ND	ND	ND
		Min	12,621	25,467	2,074	10,942	1,530	ND	ND	ND	ND	ND	ND	ND	ND	ND	ND	ND	ND	ND	ND	ND	ND	0.84	ND	ND	ND
		Max	38,362	79,493	11,336	39,655	5,657	ND	ND	ND	ND	ND	ND	ND	ND	ND	ND	ND	ND	ND	ND	ND	ND	1.31	ND	ND	ND
Bastnesite (Bst)																											
LA-ICPMS, thin section GNMH	1		6,874	11,626	1,139	3,847	229	8	385	8	4	0.40	10	0.05	0.41	0.05	9	127	3	23,724	408	24,141	6.10	0.95	0.13	4.51	549.81
LA-ICPMS, thin section GNJJ	2		58,951	76,565	10,272	37,807	4,104	304	3,120	118	241	22	86	2	13	1	628	32,330	72	188,002	3,603	192,232	5.47	0.71	0.40	2.15	139.49
			50,212	63,908	8,479	29,293	3,014	234	2,314	82	141	13	63	1	8	1	354	28,555	42	155,141	2,623	158,117	6.20	0.71	0.42	2.50	165.81
Titanite (Ttn)																											
LA-ICPMS, thin section GNJJ	5	Average	517	2,691	633	4,114	1,573	390	1,304	213	1,271	232	649	98	645	73	6,706	58	278	9,918	4,485	21,108	0.24	1.07	1.33	0.05	1.15
		±σ	97	513	123	884	445	57	420	70	405	67	179	24	137	13	1,739	19	45	1,972	1,313	4,846	0.03	0.01	0.28	0.01	0.12
		Min	406	2,115	505	3,344	1,276	315	1,011	165	989	183	515	78	538	64	5,469	38	224	8,086	3,603	17,349	0.20	1.06	1.00	0.04	1.03
		Max	594	3,144	783	5,424	2,320	461	2,018	333	1,967	347	956	139	882	96	9,720	78	321	12,709	6,738	29,167	0.28	1.08	1.67	0.07	1.32
Apatite (Apt)																											
LA-ICPMS, thin section GNJJ	1		114	366	70	447	152	71	154	21	117	23	64	9	55	9	732	5	18	1,219	451	2,402		0.94	2.18	0.11	1.61
LA-ICPMS, thin section GNMH	14	Average	15.68	92.13	25.18	200.51	91.22	19.48	110.34	18.37	111.00	21.65	56.58	6.84	39.07	5.43	611.18	0.08	10.17	444.2	369.3	1,424.7	0.13	1.07	0.97	0.02	1.69
		±σ	19.85	96.95	22.73	145.96	39.31	8.90	37.63	6.39	39.83	7.67	19.51	2.32	13.16	1.76	213.30	0.16	5.27	326.3	163.1	598.3	0.08	0.08	0.47	0.03	0.59

Geochemistry, Geophysics, Geosystems

10.1029/2018GC007453

Table 2. (continued)

Mineral method, sample	Number of analyses		La (μg/g)	Ce (μg/g)	Pr (μg/g)	Nd (μg/g)	Sm (μg/g)	Eu (μg/g)	Gd (μg/g)	Tb (μg/g)	Dy (μg/g)	Ho (μg/g)	Er (μg/g)	Tm (μg/g)	Yb (μg/g)	Lu (μg/g)	Y (μg/g)	Th (μg/g)	U (μg/g)	∑LREE (μg/g)	∑HREE (μg/g)	∑REY (μg/g)	LREE/ $HREE_N$	Ce/ Ce*	Eu/ Eu*	La/ Sm_N	Gd/ Yb_N
		Min	1.08	6.03	1.90	22.35	26.84	6.93	63.91	9.97	57.65	11.21	29.62	3.74	21.78	3.25	324.11	0.00	3.48	70.1	201.2	768.9	0.03	0.96	0.53	0.00	1.29
		Max	75.12	313.59	73.17	486.18	155.96	37.82	167.80	31.20	197.19	37.91	96.31	11.17	59.87	8.17	1,054.91	0.62	22.13	1,070.4	609.2	2,047.7	0.27	1.16	1.85	0.08	3.01
Monazite (Mnz)																											
EPMA, streambed sediment	60	Average	121,867	249,084	26,861	86,262	15,070	<DL	29,541	<DL	<DL	<DL	<DL	<DL	<DL	<DL	6,634	46,894	1,538	499,144	<DL	<DL	ND	ND	ND	ND	ND
		$\pm\sigma$	16,508	18,593	2,971	11,942	4,945	<DL	4,495	<DL	<DL	<DL	<DL	<DL	<DL	<DL	3,896	20,305	1,056	26,886	<DL	<DL	ND	ND	ND	ND	ND
		Min	87,740	207,806	20,080	60,100	9,129	<DL	19,781	<DL	<DL	<DL	<DL	<DL	<DL	<DL	394	10,633	0	419,323	<DL	<DL	ND	ND	ND	ND	ND
		Max	154,761	289,084	35,460	121,829	28,742	<DL	44,073	<DL	<DL	<DL	<DL	<DL	<DL	<DL	24,962	139,727	5,024	558,093	<DL	<DL	ND	ND	ND	ND	ND
LA-ICPMS, streambed sediment	25	Average	136,267	237,470	25,428	95,457	16,172	581	11,553	1,228	4,582	605	1,053	79	326	27	14,101	45,224	1,157	511,376	19,453	544,931	3.50	0.92	0.21	1.51	34.38
		$\pm\sigma$	13,881		2,086	16,684	6,714	569	5,737	741	2,967	413	717	59	244	21	9,273	24,017	995	17,185	10,513	35,100	1.76	0.03	0.20	0.70	29.44
		Min	111,269		22,624	75,527	7,556	104	4,892	348	1,052	134	265	13	47	3	3,177	7,834	74	491,187	6,800	511,127	1.21	0.87	0.03	0.52	10.44
		Max	158,159		31,046	143,157	34,419	2,647	27,925	3,304	12,684	1,590	2,528	185	757	58	354,86	111,685	3,470	567,616	49,031	652,133	7.73	0.99	1.12	3.14	120.24
Xenotime (Xnt)																											
LA-ICPMS, streambed sediment	8	Average	110	930	343	3,921	5,334	542	16,386	5,068	41,879	10,496	31,978	4,576	30,554	3,903	309,621	3,129	2,844	11,180	144,841	465,642	0.008	1.09	0.27	0.00	0.32
		$\pm\sigma$	20	125	37	328	459	297	702	260	2,016	269	1,251	446	4,097	592	0	1,406	718	1,024	7,507	8,191	0.001	0.04	0.14	0.00	0.05
		Min	75	680	269	3,251	4,593	196	14,948	4,661	37,966	9,897	29,964	3,751	25,035	3,031	309,621	1,499	1,942	9,205	133,300	453,509	0.007	1.07	0.10	0.00	0.27
		Max	142	1,129	403	4,445	6,061	939	17,557	5,513	44,306	10,722	33,468	5,058	36,091	4,390	309,621	5,919	3,850	12,442	154,311	475,645	0.009	1.18	0.44	0.00	0.38
Thorite (Thr)																											
EPMA, streambed sediment	3	Average	4,775	11,156	4,358	9,545	7,231	1,131	6,015	<DL	6,622	<DL	<DL	<DL	<DL	<DL	112,131	556,870	16,131	32,503	10,430	155,063	ND	ND	ND	ND	ND
		$\pm\sigma$	968	2,403	<DL	5,002	767	64	4,660	<DL	1,602	<DL	<DL	<DL	<DL	<DL	22,590	31,565	15,345	13,653	8,443	503	ND	ND	ND	ND	ND
		Min	4,093	8,623	<DL	3,772	6,688	1,086	694	<DL	5,489	<DL	<DL	<DL	<DL	<DL	98,193	534,754	7,140	16,744	694	154,679	ND	ND	ND	ND	ND
		Max	5,883	13,404	<DL	12,603	7,773	1,176	9,370	<DL	7,755	<DL	<DL	<DL	<DL	<DL	138,195	593,018	33,849	40,749	15,736	155,633	ND	ND	ND	ND	ND

[a]The UCC-normalized ratios and anomalies are also reported.

Table 3
LREE, HREE, Y, U, and Th Abundances in the Different Gneiss-Forming Accessory Minerals[a]

∑LREE	µg/g	∑HREE	µg/g	Y	µg/g	Th	µg/g	U	µg/g
Mnz	505,000	Xnt	145,000	Xnt	305,000	Thr	560,000	Thr	16,100
Bst	170,000	Thr	116,000	Thr	114,000	Mnz	46,000	Xnt	2,800
Aln	190,000	Mnz	19,500	Mnz	14,100	Bst	30,000	Mnz	1,300
Xnt	11,200	Ttn	4,500	Ttn	6,700	Xnt	3,100	Ttn	300
Ttn	10,000	Aln	4,400	Aln	1,000	Aln	730	Aln	170
Thr	9,000	Bst	3,000	Zrn	700	Ttn	60	Zrn	160
Apt	450	Zrn	520	Apt	600	Zrn	60	Bst	50
Epd	50	Apt	370	Bst	500	Na-Plg	0.40	Apt	10
Na-Plg	20	Epd	35	Epd	50	Epd	0.20	Epd	0.25
Zrn	12	Bit	25	Bit	25	Bit	0.10	Bit	0.15
Bi	12	Na-Plg	2	Na-Plg	3	Apt	0.10	Na-Plg	0.10

[a]The mineral abbreviations are used in the table as follows: Mzn = monazite, Xtn = xenotime, Thr = thorite, Zrn = zircon, Apt = apatite, Epd = epidote, Na-Plg = Na-plagioclase, Bi = biotite, Aln = allanite, Bst = bastnesite, and Ttn = titanite.

4.3. Ferralsol and Vertisol

4.3.1. Soil Composition

The UCC-normalized patterns are displayed in Figure 8. In the ferralsol and vertisol profiles, the average elemental contents (in µg/g) are similar with 155 and 124 of REY, 1.2 and 1.1 of U, 9.1 and 6.9 of Th, and 147 and 120 of P, respectively (Table 1). The UCC-normalized patterns for the soil profiles (Figure 8) show variable and significant ranges of Ce-anomalies from positive to negative ($0.3 < Ce/Ce^* < 3.0$) and Gd/Yb_N (0.5–1.2) and slight for Eu-anomalies ($0.9 < Eu/Eu^* < 1.2$) and La/Sm_N (0.6–1.1).

4.3.2. Soil Mineralogy

The ferralsol matrix is composed of clay minerals (mainly kaolinite), iron oxides, and oxyhydroxides (mainly goethite) with abundant primary resistant crystals of amphibole, Na-plagioclase, K-feldspars, epidote, and quartz (Braun et al., 2009). At 100–120 cm depth, the brighter crystals in BSE encompass tiny grains (less than 10 µm) of sulphides (Fe, Pb), sulphates (Ba), oxides (Fe, Ti, Cr, Zr), and carbonates (Pb). Crystals of secondary rhabdophane ($LREEPO_4.nH_2O$) and residual zircon ($ZrSiO_4$) between 1 and 5 µm in length were observed. In the deeper horizon (300–320 cm), the same minerals with similar grain sizes are also found. In addition, authigenic LREE carbonates and cerianite (CeO_2) are also present along with resistant xenotime (YPO_4).

4.3.3. Soil Elemental Extractions

The results of the soil extraction experiments including the elemental contents (REY, U-Th, Zr-Ti, and Fe-Ca-Na-P) for bulk sample analyses (fusion for both bulk and sand size fraction and acid digestion for silt + clay and clay size fractions) and leaching experiments (NH_4Ac 1 *M*, HCl 0.5 *M*, and HCl 5 *M*), are listed in supporting information Data set S5.

The estimates of cumulative per cent of recovery (PER) and the residual part (REL) for both bulk and grain size fractions are also reported. The ferralsol WP1 100–120 cm and vertisol WP5 100–120 cm are composed of 34% and 26% of sand, 15% and 25% of silt, and 51% and 49% of clays, respectively. The bar graphs of Figure 9 display the respective PERs and REL for the bulk soil samples and the different grain size fractions for ferralsol and vertisol, respectively.

The Fe reservoir is mostly located in the silt + clay size fraction. In both bulk soil samples, Fe reservoir is allocated by decreasing order within the well-crystallized oxides and oxyhydroxides ($PER_{Fe\text{-}HCl5M\text{-}ferral.} \approx PER_{Fe\text{-}HCl5M\text{-}vert.} = 62–63\%$), the poorly crystallized oxides and oxyhydroxides ($PER_{Fe\text{-}HCl0.5M\text{-}ferral.} = 35\%$; $PER_{Fe\text{-}HCl0.5M\text{-}vert.} = 18\%$) and the residual pool ($REL_{Fe\text{-}ferral.} = 3\%$; $REL_{Fe\text{-}vert.} = 19\%$). In both bulk soil samples, the Ca reservoir is mostly distributed between the cation exchangeable pool ($PER_{Ca\text{-}NH4Ac\text{-}ferral.} = 51\%$; $PER_{Ca\text{-}NH4Ac\text{-}vert.} = 38\%$) and in the residual pool ($REL_{Ca\text{-}ferral.} = 34\%$; $REL_{Ca\text{-}vert.} = 49\%$) attesting the presence of residual plagioclase and amphibole crystals. The P and Na reservoirs are both slightly recovered from the HCl 5 *N* extraction, the larger parts remaining in the residual pool (plagioclase crystals for Na). The Zr and Ti reservoirs essentially remain in the residue and hence are kept in resistant insoluble minerals (e.g., zircon, TiO_2).

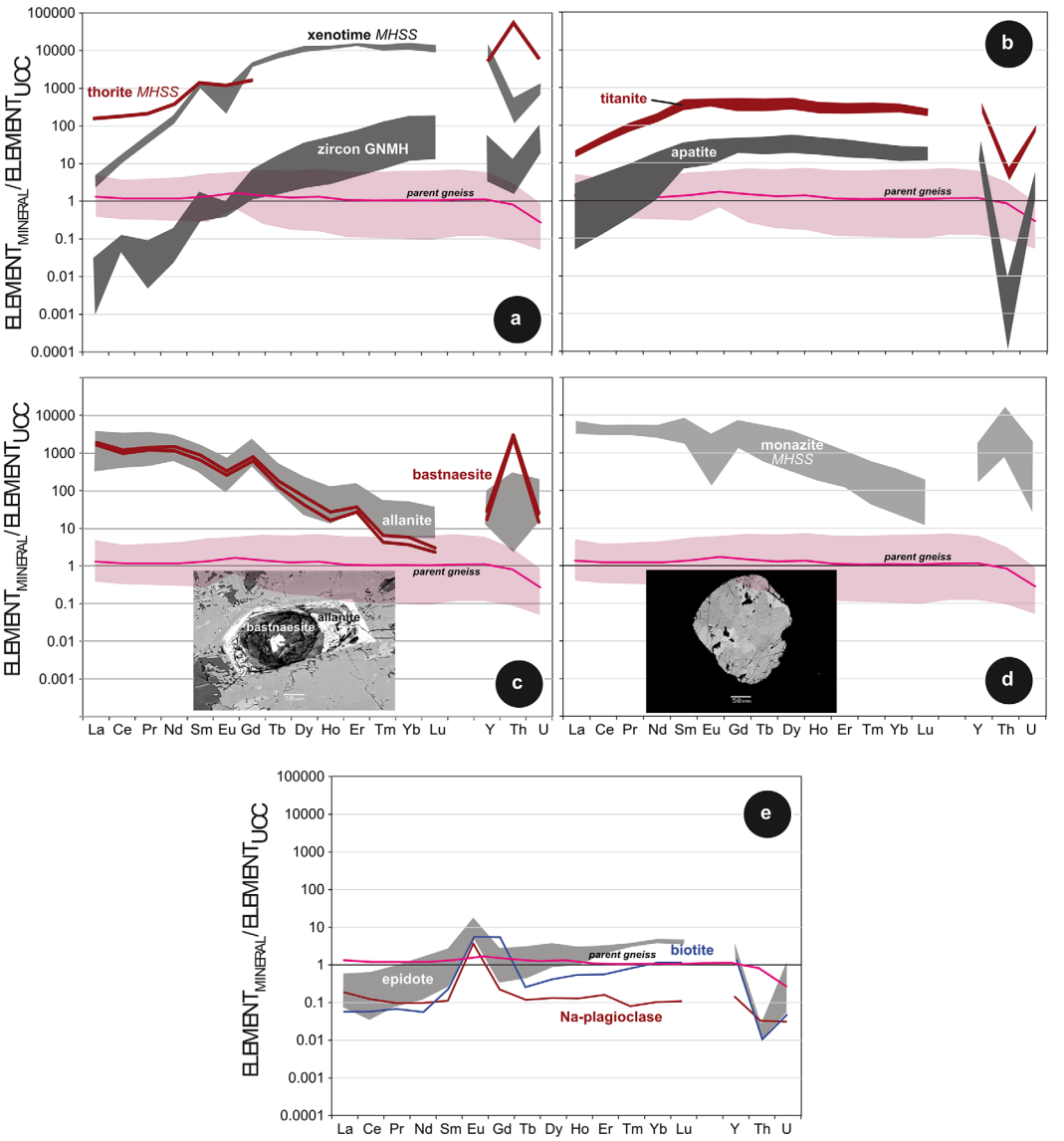


Figure 5. UCC-normalized REY-Th-U patterns of accessory minerals: (a) xenotime, thorite and zircon, (b) titanite and apatite, (c) allanite and bastnesite, (d) monazite and major minerals, (e) epidote, Na-plagioclase and biotite from gneissic samples (GNMH, MHSS). The shadowed areas represent the variability. The UCC-normalized REY-Th-U pattern for average gneiss (GNAV) and its variability are added.

Both LREE-Ce (i.e., LREE minus Ce) reservoirs are accumulated in the silt + clay size fractions while Ce is in the sand size fraction associated with Na. In both soils, the LREE-Ce reservoirs are mostly accumulated within the poorly crystalized iron oxides and oxy-hydroxides ($PER_{LREE\text{-}Ce\text{-}HCl0.5M\text{-}ferral.} = 75\%$; $PER_{LREE\text{-}Ce\text{-}HCl0.5M\text{-}vert.} = 59\%$) rather than the well-crystallized ones ($PER_{LREE\text{-}Ce\text{-}HCl5M\text{-}ferral.} = 24\%$; $PER_{LREE\text{-}Ce\text{-}HCl5M\text{-}vert.} = 26\%$). The LREE-Ce reservoir linked to ion-exchangeable pool is very low ($PER_{LREE\text{-}Ce\text{-}NH4Ac\text{-}1M} \approx 1\%$). The allocation of HREE is similar to that of LREE-Ce with most of the reservoir in the poorly crystalized iron oxides and oxy-hydroxides. However, both $PER_{HREE\text{-}HCl5M}$ and $PER_{HREE\text{-}HCl0.5M}$ decrease as the HREE atomic numbers increase. Correspondingly, the residual parts increase toward the heaviest HREE ($REL_{HREE\text{-}ferral.} = 11\%$; $REL_{HREE\text{-}vert.} = 28\%$). The allocation of Y is similar to those of HREE (Tb-Dy).

Most of the Th reservoir is located in the silt + clay size fraction. About one third of Th remains in the residual pool ($REL_{Th\text{-}ferral.} = 31\%$ and $REL_{Th\text{-}vert.} = 34\%$). Th is mostly extracted by HCl 5 *M* (well-crystallized oxides and oxy-hydroxides). The main U reservoir is located in the silt + clay size fraction. A large fraction remains

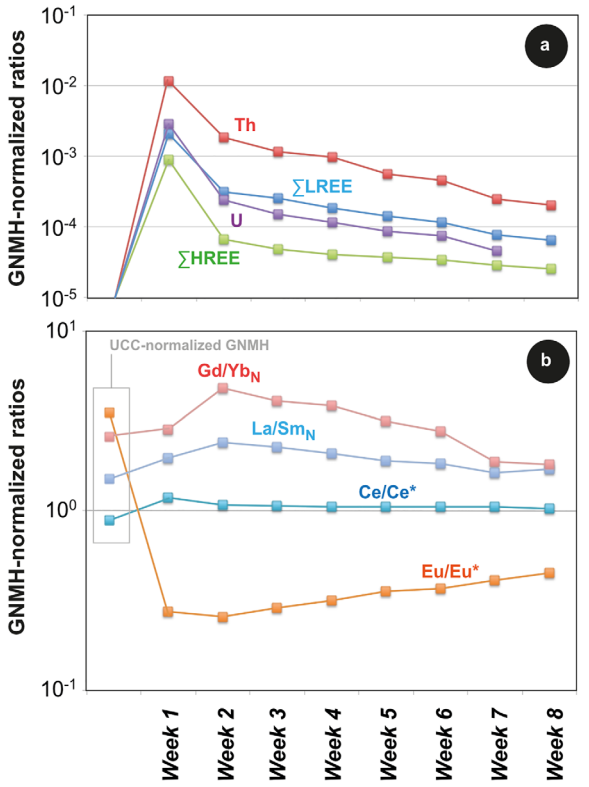


Figure 6. Evolution of the composition of leucocratic gneiss (GNMH) acid leaching experiments normalized to GNMH: (a) LREE, HREE, Th, and U, (b) La/Sm, Gd/Yb, Ce/Ce*, and Eu/Eu*.

in the residual part ($REL_{U\text{-}ferral.}$ = 52% and $REL_{U\text{-}vert.}$ = 75%). U is mostly extracted by HCl 0.5 *N* (poorly crystallized oxides and oxy-hydroxides).

4.4. Streambed and Suspended Sediments Composition

The statistics for the streambed and suspended sediment REY-Th-U contents are reported in Table 1 and the UCC-normalized patterns in Figure 10. The suspended sediment composition is constant irrespective of the sampling period of the year. The average contents (in μg/g) are of 135 ± 7 for ∑REY, 7.5 ± 0.3 for Th and 1.4 ± 0.2 for U. Their UCC-normalized patterns show a slight depletion in LREE, Th and U close to those of the clay + silt size fraction of both vertisol and ferralsol. However, there is a discrepancy with respect to the Ce anomaly. The suspended sediment patterns do not show any Ce-anomaly while the clay + silt size fraction of ferralsol displays a positive Ce-anomaly and vertisol show a negative Ce-anomaly. Compared to bulk soils and suspended sediments, the streambed sediment REY-Th-U contents are very low with average (in μg/g) of 28 ± 4 for ∑REY, 0.3 ± 0.1 for U and 1.3 ± 0.5 for Th. The UCC-normalized pattern of streambed sediments is similar to those of the fine sand grain size fraction of both vertisol and ferralsol however, in contrast, has a stronger positive Ce-anomaly.

5. Discussion

5.1. REY-Th-U Bearing Mineral Assemblage in Gneiss, Elemental Contribution, and Sensitivity to Chemical Weathering

5.1.1. Effect of Hydrothermal Fluids on the Paragenesis of the REY-Th-U Bearing Accessory Suite

The presence of detrital, rounded monazite and xenotime grains in the streambed sediments clearly points out that both minerals do exist in unidentified gneissic domains at the watershed scale. Though, we neither observe any of these minerals in thin sections nor in parent gneiss mineral separates, we can reasonably argue that magmatic monazite crystals may have been incompletely replaced into allanite and apatite during hydrothermalism event. Numerous studies reported that the replacement of magmatic monazite by allanite and apatite is a common feature. For instance, partial replacement of accessory magmatic monazite by allanite-apatite-epidote paragenesis was observed in peraluminous granite metamorphosed under amphibolite facies conditions (Finger et al., 1998). Electron microprobe analyses suggest that P, REY, Th and U released from monazite breakdown were redistributed in the newly formed allanite, apatite and epidote, thus supporting the hypothesis that these trace elements were highly immobile during metamorphism. Finger et al. (1998) also showed that the monazite stability strongly depends on the armoring of the crystals by minerals with low intracrystalline diffusion coefficient. Late low-temperature alteration also affects the stability of monazite (Berger et al., 2008; Poitrasson et al., 2000; Seydoux-Guillaume et al., 2012). Berger et al. (2008) thoroughly described late low-temperature alteration of monazite and allanite in magmatic and metamorphic rocks of Madagascar associated with micro-fissures predominantly affecting the accessory minerals. They found that monazite and thorite were replaced by thorogummite (Th,U)[$(SiO)_4(OH)_4$] and rhabdophane ($LREEPO_4H_2O$), respectively, and allanite was replaced by bastnesite ($LREECO_3F$). Furthermore, Th-rich minerals (monazite, thorite) were more affected by alteration than Th-poor phases, probably due to the effect of metamictization. In the hydrothermally altered Soultz monzogranite, Middleton et al. (2013) also reported the conditions for

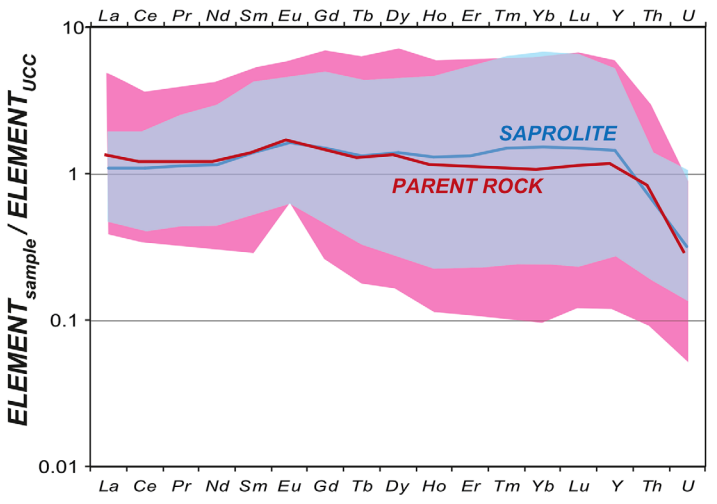


Figure 7. UCC-normalized REY-Th-U patterns for the average saprolite and parent gneiss. The shadowed areas (rose for saprolite and purple for gneiss) represent the variability.

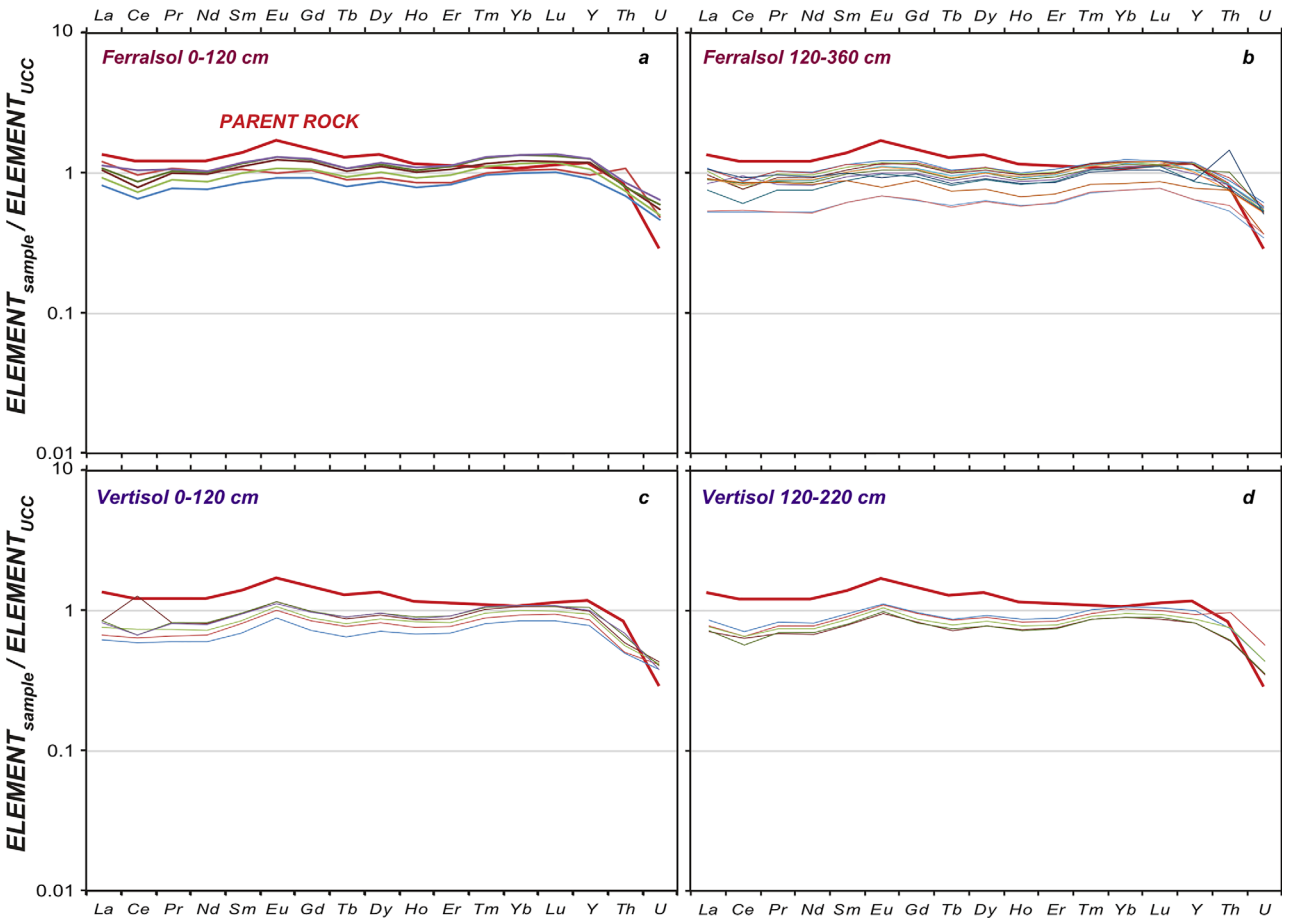


Figure 8. UCC-normalized REY-Th-U patterns for the soil cover with ferralsol (WP1) between (a) 0 and 120 cm and (b) 120 and 360 cm and vertisol (WP5) between (c) 0 and 120 cm and (d) 120 and 220 cm. The average parent gneiss pattern is also indicated (red line).

accessory mineral destabilization and the complexity of secondary assemblages. Allanite crystals were also later affected by CO_3-F rich pervasive hydrothermal fluids and replaced by bastnesite and an amorphous alumina-silicate phase, the bastnesite crystals being enriched in Th as compared to allanite. Phosphates or fluoro-carbonates dominate the alteration products of titanite. It is thus germane to argue that both metamorphism and hydrothermal activity profoundly modified the REY-Th-U accessory assemblage at the Mule Hole watershed scale with various intensities and timings.

5.1.2. Control of REY-Th-U Reservoir by Primary Bearing Minerals and Their Breakdown Aptitude

In order to quantitatively establish which are the minerals controlling the availability of the REY-Th-U reservoir to chemical weathering at the watershed scale, we estimate the modal abundances of the REY-Th-U bearing minerals (monazite, xenotime, allanite, bastnesite, titanite, and apatite; see Table 3) with a linear inverse method using least squares criterion (Tarantola & Valette, 1982). The solution and error are given by equations (47) and (48) in Tarantola & Valette (1982):

$$\hat{x} = \left(A^T \cdot C_{y_0 y_0}^{-1} \cdot A\right)^{-1} \cdot C_{y_0 y_0}^{-1} \cdot y_0$$

$$C_{\hat{x}x} = \left(A^T \cdot C_{y_0 y_0}^{-1} \cdot A\right)^{-1}$$

Where y_0 is the chemical composition vector of the rock, A is the matrix of the mineral compositions and $\hat{x}$ is the a posteriori solution (modal abundance vector), $C_{y_0 y_0}^{-1}$ is the inverse of the covariance matrix and $C_{\hat{x}x}$ is the a posteriori error covariance of the solution. The residuals are calculated by $y_0 - \hat{y}$, where $\hat{y} = A\hat{x}$.

From the observation that streambed sediments only contain monazite and xenotime grains as resistant REY-Th-U bearing minerals, it can be deduced that weathering processes completely breakdown allanite, bastnesite,

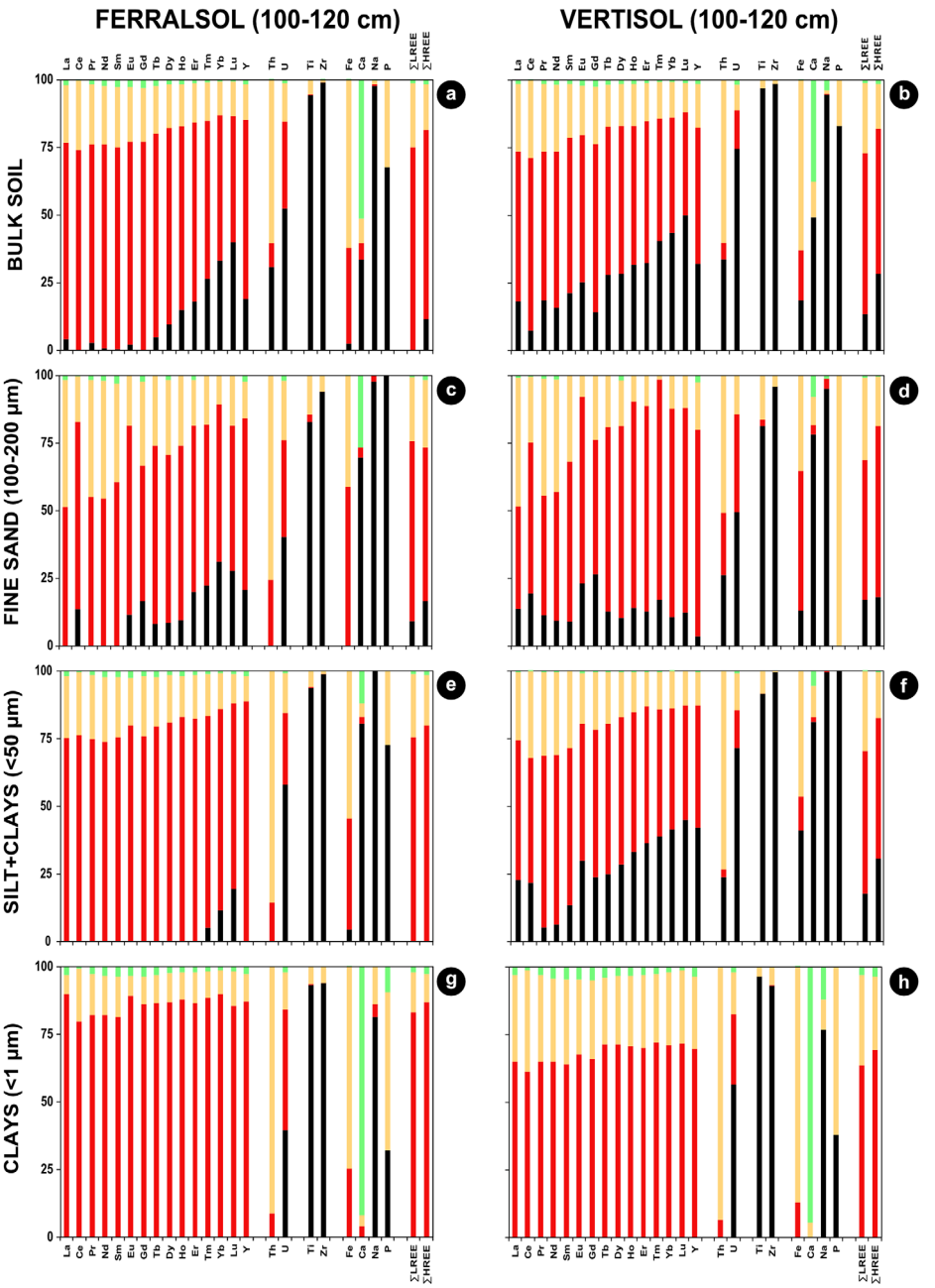


Figure 9. Cumulative bar graphs for the extraction experiments for ferralsol (WP1 100–120 cm) and vertisol (WP5 100–120 cm): (a, b) bulk soil, (c, d) fine sand size fraction, (e, f) silt + clay size fraction, and (g, h) clay size fraction. The graphs display the elemental proportions recovered from the exchangeable pool (light green), the well (orange) and poorly (red) crystallized oxides and oxyhydroxides pools and the residual pool (black).

titanite, and apatite in the regolith. Assuming that the REY-Th-U contained in monazite and xenotime crystals at the watershed scale is not affected by weathering processes (Sengupta & Gosen, 2016), this latter has to be deduced from the available pool. Hence, the matrix y_0^* of the elemental contents ($[E]_{Mnz+Xnt}$) with $E = LREE, HREE, Y, U, Th$ related to these resistant minerals in the average gneiss (GNAV) is determined by:

$$[E]_{Mnz+Xnt} = \frac{\rho_{soil_average} \cdot [E]_{\text{stream_sed}}}{\rho_{GNAV} \cdot [E]_{GNAV}}$$

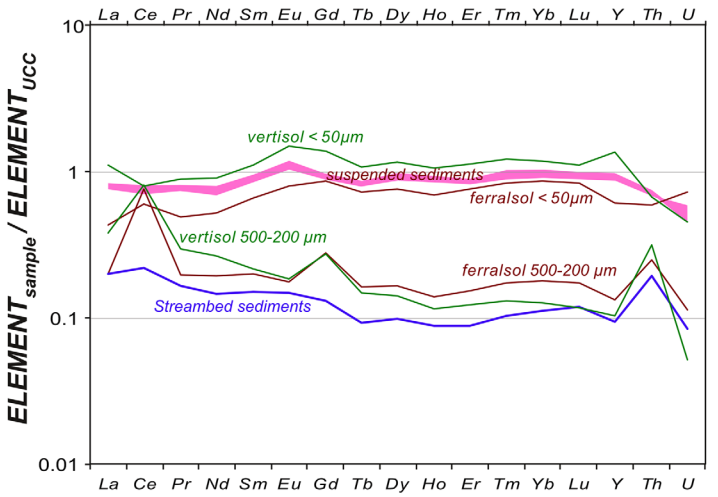


Figure 10. UCC-normalized REY-Th-U patterns for the suspended and streambed sediments compared to the patterns of soil grain size fractions (silt + clays and fine sand) from ferralsol and vertisol at 100–120 cm depth.

where $[E]_{GNAV}$ and $[E]_{stream_sed}$ are the average contents of LREE, HREE, Y, U, and Th (in µg/g) in the parent gneiss (GNAV) and in the bulk stream sediment (SSAV) and ρ_{GNAV} and $\rho_{soil_average}$ the densities of the gneiss and of the bulk soil cover, respectively. We assume that the streambed sediments are derived only from the erosion of the first 2 m of regolith at the watershed scale. Estimated modal abundances of monazite and xenotime at the watershed scale are very low with values of 3.3×10^{-3} vol% and 2.6×10^{-4} vol%, respectively (Table 4).

We then corrected the values $(y_0 - y_0^*)$ from parent gneiss to estimate the modal abundances of the other minerals: allanite, bastnesite, titanite and apatite (matrix A^*). Table 4 sums up the bulk compositions and standard deviations (GNAV, SSAV), calculated modal abundances and their errors, estimated bulk compositions ($\hat{y}$) and associated residuals, and the contributions from each mineral to the whole rock. The control of zircon on elemental reservoirs is insignificant and is not reported in the Table 4.

Both resistant monazite and xenotime account for about 10% of the LREE and HREE reservoir, about 14% of the Th and Y reservoir but only 7% of the U reservoir. Both minerals are prone to relative accumulation within the weathering profile leading to potential accumulation of REY-Th-U. The reactive accessory minerals, broken down during the first stage of weathering, are then able to release 86% of Th and Y, 90% of REE (except Eu) and 93% of U (Table 4). Allanite dominates for LREE (51%), titanite for HREE (66%), Y (77%) and U (78%) and bastnesite for Th (81%). Apatite controls only 12% of the whole REY-Th-U reservoir. Moreover, an estimate based on the gneiss modal abundance of Na-plagioclase (38 ± 11%vol; Braun et al., 2009) indicates that this mineral accounts for about 60% of the Eu reservoir (low Eu concentration but elevated modal abundance). Therefore, the Na-plagioclase breakdown will have an impact on Eu mobility and transfer, inferred from the magnitude of the Eu-anomaly in the fluids. The leaching experiments of the hydrothermalized leucocratic gneiss end-member (GNMH), free of

Table 4
REY-Th-U Average Composition of the Gneiss, Stream Sediments, and Modal Abundances and Contribution to the Whole Rock of Main REY-Th-U Bearing Accessory Minerals at the Watershed Scale

	n	Density (g/cm^3)	∑LREE (µg/g)	∑HREE (µg/g)	Y (µg/g)	U (µg/g)	Th (µg/g)
Average gneiss (y_0)	33	2.74	161.0	16.9	23.6	0.8	8.7
±σ		0.05	107.4	16.3	22.7	0.5	6.2
Average stream sediments	4	1.77	22.4	2.3	3.3	0.3	1.3
±σ		0.21	3.8	0.6	1.0	0.1	0.5
y*			14.48	1.48	2.13	0.17	0.84
Estimate			14.53	1.57	2.58	0.05	1.30
Residual			0.11	0.09	0.45	−0.12	0.46
$y_0 - y^*$			146.5	15.4	21.5	0.6	7.8
Estimate			145.3	12.8	15.7	0.7	7.9
Residuals			−1.2	−2.6	−5.8	0.1	0.0

	Mode %	±σ	Mineral contribution to the whole rock composition (%) LREE	HREE	Y	U	Th
Aln	0.04	0.06	51	13	2	10	3
Bst	0.02	0.02	27	6	1	2	81
Ttn	0.23	0.16	13	66	77	78	1
Apt	0.17	0.06	0	4	6	2	0
Mnz	3.3E-03	2.0E-06	9	4	2	4	14
Xnt	2.6E-04	2.9E-06	0	7	12	3	0
% of REY-Th-U prone to chemical weathering (Aln + Bst + Ttn + Apt)			91	89	86	93	86

resistant monazite and xenotime, show, in the first step, a quick breakdown of the accessory minerals with significant negative Eu-anomalies ($0.1 < Eu/Eu^* < 0.4$), likely allanite and bastnesite. The increase of the Eu/Eu* at the end of the experiment indicates the slight dissolution of Na-plagioclase ($Eu/Eu^* = 28$).

5.2. Long-Term Fractionation and Redistribution of REY-Th-U

In order to discuss the fractionation and redistribution of REY-Th-U in the regolith on a long-term basis, we combined open-system mass fraction transport function $\tau_{j,w}$ based on bulk analyses with the results of both mineralogical investigations and soil leaching experiments. Figure 11 displays the elemental loss/gain depth profiles.

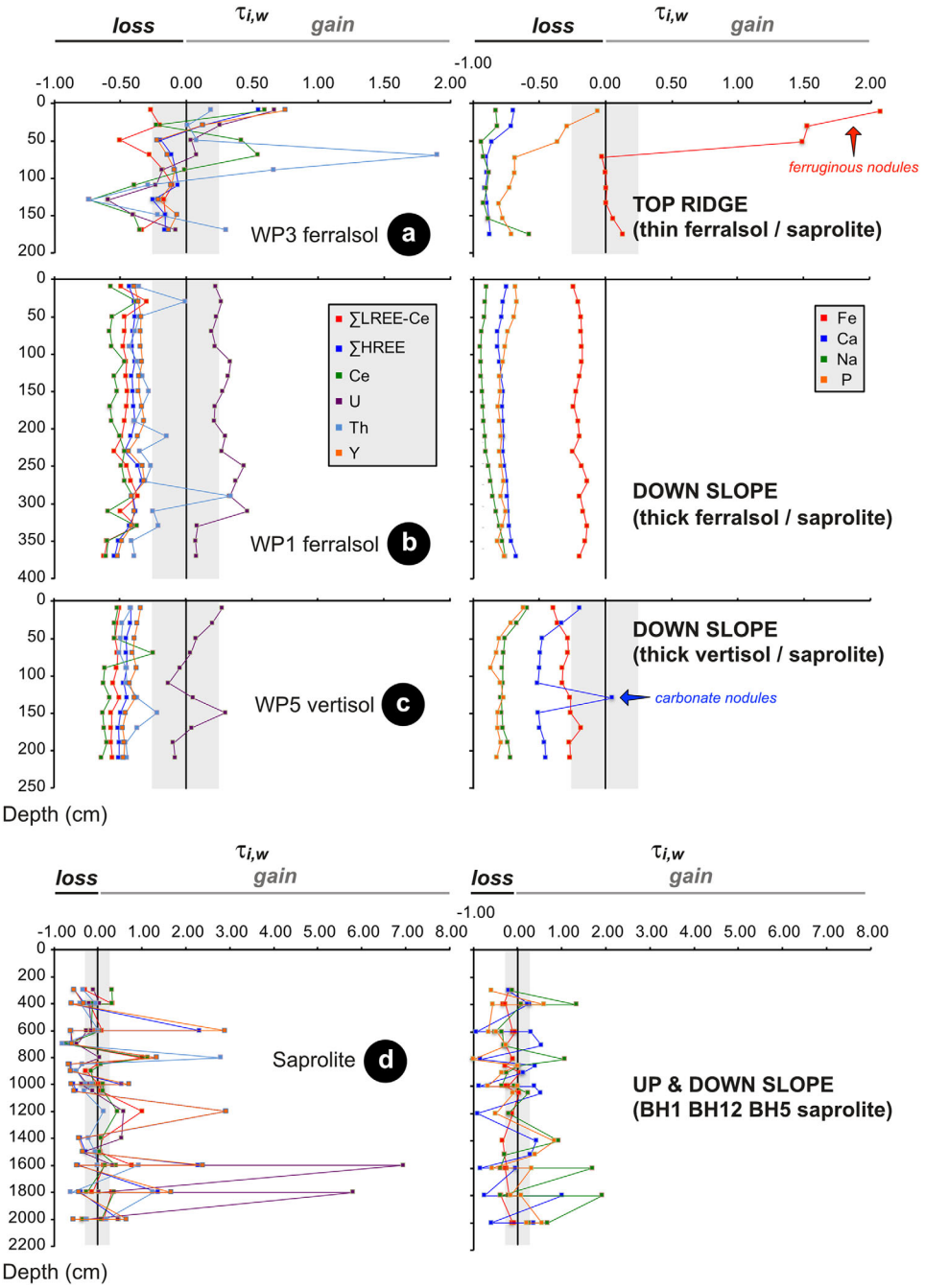


Figure 11. Calculated τ for LREE-Ce (LREE minus Ce), Ce, HREE, Y, Th, U, and selected major elements (Fe, Ca, Na, P) referenced to Ti in (a) the thin ferralsol/saprolite depth profile of ridge top (WP3), (b,c) thick ferralsol/saprolite and vertisol/saprolite depth profiles from downslope (WP1 and WP5), and (d) the saprolite of BH1, BH12, and BH5.

5.2.1. Rare Earth Elements

In the ridgetop saprolite (Figures 11a and 11d), the LREE-Ce (LREE minus Ce), Ce, HREE, and Y elemental loss/gain depth profiles are erratic with spikes. The significant variation on the open-system mass fraction transport functions ($\tau_{j,Ti}$) is due to the heterogeneity in the accessory mineral distribution within the parent gneiss. Overall, the REY losses are not significant in the saprolite and fall mostly in the $\pm$20% error range attested by the very low exports of LREE and HREE by the groundwater at the weathering front (Braun et al., 2017).

In the ferralsol profile WP1 (downslope) and vertisol profile WP5 (valley), the depth profiles for LREE-Ce, HREE, and Y are rather uniform with losses of around $-$40% and $-$50% on an average (Figures 11b and 11c). For the vertisol profile WP5, the depletion $\tau_{j,w}$ profiles were already presented in Violette et al. (2010b). Compared to the previous calculations, the displayed $\tau_{j,w}$ values slightly differ due to the re-evaluation of the Ti content of the average gneiss (2,377 μg/g instead of 2,018 μg/g in the former calculation, leading to a shift of +15%, within the limits of the error bars of 20% for the mass balance). By contrast, within the eroded ridgetop profile WP3, the LREE-Ce, HREE, and Y loss/gain depth profiles are erratic with spikes alike in the underlying saprolite (BH5). The soil profiles are, on average, depleted in LREE-Ce and HREY with significant average losses ($\tau_{LREE-Ce,Ti} = -49\% \pm 7$) and ($\tau_{HREY,Ti} = -43\% \pm 5$), respectively. Irrespective of the soil profile, the $\tau_{Ce,Ti}$ depth profiles display significant peaks corresponding to positive Ce-anomalies related to the accumulation of cerianite (Braun et al., 1998a), with the most pronounced Ce/Ce* reaches 3.0 (WP3). These losses are of the same magnitude for redox-sensitive Ce ($\tau_{Ce,Ti} = -53\% \pm 9$).

In the soil cover, the LREE-Ce reservoir is controlled by poorly crystallized secondary Fe oxides and oxyhydroxides, pH-dependent secondary phosphate minerals, and climate-sensitive pedogenic carbonates (Violette et al., 2010b). The residual LREE pool (i.e., resistant monazite) does not control a significant amount of LREE, which is, however, more important for vertisol (10%), than for ferralsol (< 1%). The poorly crystallized secondary Fe oxides and oxyhydroxides similarly control HREY (Figure 9) while the resistant phases, likely xenotime, control about 30% of HREY in vertisol against only 10% in ferralsol.

For LREE-Ce, even if the presence of rhabdophane is observed, aluminous phosphates of the alunite supergroup, crandallite subgroup can also be foreseen (e.g., La-florencite [$(La)Al_3(PO_4)_2(OH)_6$]; Braun et al., 1990, 1998a). The contribution of pedogenic carbonates to the LREE-Ce reservoir can be assessed by taking into account the average $CaCO_3$ contents in the bulk soil samples. In the soil profiles, the $CaCO_3$ contents range from below the detection limit (<1 g/kg) to maximum values of 1.2 g/kg in the ferralsol (WP1) and 15.5 g/kg in the vertisol (WP5). The average LREE-Ce content of 1 g of $CaCO_3$ is about of 320 $\pm$ 280 μg/g (Violette et al., 2010b). Assuming an average $CaCO_3$ content of 1 g/kg within vertisol and ferralsol profiles, the LREE-Ce reservoir contained in pedogenic carbonates is about 1%, meaning that these authigenic minerals do not exert a significant control on LREE-Ce dynamic in the soil cover. Subsequently, simplified calculation carried out to allocate the LREE-Ce reservoir between the iron phases and phosphate minerals assuming that (i) all P is in rhabdophane [$(La)PO_4 \cdot (H_2O)$, Molecular Weight = 252 g, 12.3% of P and 55.1% of La], (ii) an average P content of 140 $\pm$ 30 μg/g (0.032% of P_2O_5; Violette et al., 2010a, Appendix A) in soil, and (iii) an average La content of 26 $\pm$ 9 μg/g in soil, tell that a maximum of roughly 25% of La (less if we take into account La-florencite) is likely incorporated in rhabdophane and the remaining 75% are likely to be adsorbed/occluded on/in poorly crystallized iron oxides and oxyhydroxides. These secondary phases can incorporate Ce(III) as the other LREE. Ce(IV) can also be controlled by minerals such as Mn–Ba oxides as psilomelane or todorokite in vertisol (Violette et al., 2010b) and cerianite ($Ce(IV)O_2$) in ferralsol (this study). Coatings of cerianite on framework mineral surfaces (e.g., quartz and plagioclase grains) can explain the positive Ce-anomaly of the sand size fraction systematically found in WP1 and WP5 (supporting information Data set S5). Precipitation as secondary phosphates and/or adsorption on clays in the saprolite delays the LREE leaching in the saprolite and then from soil horizons. Moreover, REE are not available from the exchangeable pool and would not be easily available for the plant uptake by ion exchange. The plagioclase breakdown can be foreseen in groundwater by both the magnitude of the average Eu-anomaly (Eu/Eu* = 5; Braun et al., 2017) and the significant Na fluxes in the different piezometers (Riotte et al., 2014b).

5.2.2. Thorium

The noteworthy Th accumulation spikes are attributed to the initial heterogeneous distribution of the accessory minerals in the parent material. The loss of Th in ferralsol and vertisol profiles is moderate ($\tau_{Th,Ti} = -33\% \pm 17$). The soil reservoir is mostly controlled by the well-crystallized authigenic oxides and

oxyhydroxides pool (60%) and by the residual pool (30%). The solute export of Th by the groundwater is extremely low (Braun et al., 2017). Thus, we can hypothesize that Th from the breakdown of bastnesite is precipitated as pH-dependent thorianite, occluded in iron oxides and oxyhydroxides. A significant fraction is still preserved and relatively accumulated in resistant minerals (i.e., monazite). As for REE, Th is not available from the exchangeable pool.

5.2.3. Uranium

Uranium is the only element gained in the soil profiles ($\tau_{U,Ti} = +19\% \pm 16$). The most important U pools are the residual phases (50% in ferralsol and 75% in vertisol) and, to a lesser extent, the poorly crystallized iron oxides and oxyhydroxides. U is also not available from the exchangeable pool in soils. Previous studies have shown that, as for LREE-Ce, U is also enriched in pedogenic carbonates (Violette et al., 2010b) but with an estimate control less than 1% of the U reservoir. The U fraction associated with poorly crystallized iron oxides can be adsorbed or occluded in their lattice (Duff et al., 2002). If we consider now the residual part, for instance, in the ferralsol, average U content of 1 μg/g, of which 50% are in the residual part and assuming that monazite controls this reservoir, then the abundance of monazite in the soil would be 10 times than that of those of the average parent gneiss (3.3×10^{-3}% of monazite accounts for 0.05 μg/g of U, see estimate above). We can also consider that a large part of the U pool mobilized from the breakdown of titanite (78% of the parent gneiss U reservoir) is leached in the groundwater at the weathering front prior to the formation of the soil horizons. The significant groundwater solute U flux, which is 25 times more than for the stream, supports this assumption (Braun et al., 2017).

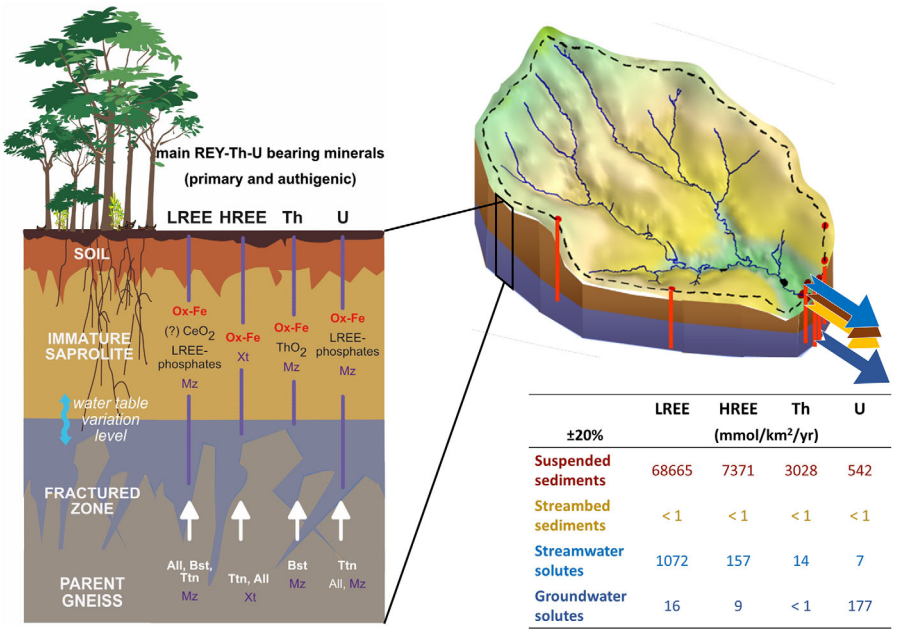
5.3. Hydrological Sorting: Solid Vs. Solute Exports and Shape of the REY-U-Th Normalized Patterns of Suspended and Streambed Sediments

At the watershed scale, the hydrological sorting of sediments by the ephemeral Mule Hole stream is driven by the intensity of the rainfall events and the turbulent flood flow. While the vegetation on slopes and valleys tends to slow down the erosion processes, the intensity of overland flow and the instability of the stream banks, on the opposite, increase them. As a result, the eroded sediments are a mixture of weathering products (e.g., kaolinite, smectite, iron oxides, and oxyhydroxides), framework minerals (quartz, plagioclase, amphibole), resistant minerals (e.g., zircon, monazite, xenotime, Ti-oxides), and vegetation debris. During the flood events, the turbulent flow mostly exports silt and clays as suspended sediments. The fine and coarse sandy sediments are deposited in the channel and are moved by rolling, sliding, and saltation.

In 2005, the suspended sediment export at the Mule Hole was 94 t/km^2/yr (±20%). The streambed transport is generally thought to be 10% of the total sediment load in a stream (Summerfield, 1991), giving an estimate of the streambed sediment export of 10 t/km^2/yr (±20%). Both values allow us to evaluate the solid fluxes of REY-Th-U. They are reported in Figure 12 along with the solute fluxes from Braun et al. (2017).

The hydrological sorting affects the distribution of REY-Th-U in different ways. The exports of LREE, HREY, and Th are, by far, dominated by the suspended sediment fluxes, which represent often more than 96% of the total exports. This solid export is mainly driven by iron oxides and oxyhydroxides (adsorption/occlusion). One striking point is that the suspended sediments do not show any Ce-anomaly although both negative and positive Ce-anomalies are present in soil horizons, especially in the fine sand grain size fractions. To explain the absence of Ce-anomaly in the suspended sediments, we argue that cerianite (CeO_2) is essentially present as nanometric crystal coatings embedding the framework minerals of sandy grain size (i.e., quartz and plagioclase grains) (Braun et al., 1998b). When these grains are transported by the draining water, the fine CeO_2 coating can be easily removed and the tiny particles of cerianite are admixed with the suspended load. The result of the mixing is the smoothing of the UCC-normalized patterns toward $Ce/Ce^* = 1$ (Figure 10). Hence the significant and widespread REE fractionation occurring during weathering processes is canceled by the hydrological sorting of sediments, which confirms the conclusions of Su et al. (2017).

Conversely, most of the U export is shared between groundwater and suspended sediment (177 and 542 mmol/km^2/yr, respectively) (Figure 10). The export by the stream sediments is dominated by adsorption/occlusion with iron oxides and oxyhydroxides.



±20%	LREE	HREE	Th	U
	(mmol/km²/yr)			
Suspended sediments	68665	7371	3028	542
Streambed sediments	< 1	< 1	< 1	< 1
Streamwater solutes	1072	157	14	7
Groundwater solutes	16	9	< 1	177

Figure 12. Schematic view of the REY-Th-U fractionation and redistribution from primary bearing to authigenic phases in the Mule Hole regolith and related solid exports (this study) and solute exports in the stream and groundwater (from Braun et al., 2017). The mineral abbreviations are: Mzn, monazite; Xtn, xenotime; Aln, allanite; Bst, bastnesite; Ttn, titanite; Ox-Fe, iron oxides and oxyhydroxides which can adsorb or occlude REY-Th-U; Nm, not measured.

6. Conclusion

The integrated study of the REY-Th-U reservoirs in the Mule Hole CZO allows us to draw the following hints:

- The main REY-Th-U bearing minerals are allanite, bastnesite, titanite, monazite, xenotime, thorite and apatite. Allanite dominates for LREE (51%), titanite for HREE (66%), Y (77%), and U (78%) and bastnesite for Th (81%), Plagioclase controls about 60% of the Eu reservoir. Metamorphism and hydrothermal activity profoundly modified this assemblage over time with various intensities at the watershed scale. The circulation of low-temperature hydrothermal fluids induced the replacement of monazite by allanite and apatite, and allanite by bastnesite.
- The mineralogical control on the REY-Th-U reservoir strongly influences the elemental redistribution within the regolith and the potential exports of these elements in the draining waters. Reactive accessory minerals (allanite, bastnesite, titanite, and apatite) are broken down in the initial stages of weathering, at the weathering front, allowing 86% (Th, Y) to 93% (U) of the elements to be mobilized and redistributed among authigenic phases (e.g., phosphates, carbonates, oxides as CeO_2 and ThO_2), adsorbed by clays and/or exported by groundwater.
- Monazite and xenotime crystals are generally preserved in the regolith and relatively accumulate before being exported in streambed sediments.
- Plagioclase breakdown has an impact on the Eu mobility and transfer, which can be inferred from the magnitude of the Eu-anomaly.
- Though somewhat preserved in the saprolite, about 50% of REY and 30% of Th are lost in the soil cover. The remaining REY-Th are mostly trapped in secondary iron-related phases (poorly crystallized for REY and well-crystallized for Th) and, to a lesser extent, in resistant minerals. They are not significantly linked to the soil exchangeable pool, which indicates that the soil reservoir of REY-Th may not be easily available for plant uptake by ion exchange. In the stream, the LREE, HREY, and Th exports are mainly exported as suspended sediments (silt and clays) rather than streambed sediments (in resistant minerals) and solutes.

- The REE fractionation by weathering with either positive or negative Ce/Ce* anomalies is smoothed in the stream suspended sediments (Ce/Ce* tends toward 1) due to hydrological sorting of silty and clayey particles.
- Most of the primary U source, located in titanite, is exported by groundwater (U flux is 25 times more than for the stream). The remaining pool in regolith is either in primary resistant minerals or associated with iron oxides and oxyhydroxides.

Acknowledgments
Data supporting text and tables are available in supporting information tables and Data Sets 1–5. The Mule Hole basin is part of the SNO-BVET project (Système National d'Observation-Bassin Versant Expérimentaux Tropicaux; https://mtropics.obs-mip.fr/experimental-tropical-watersheds-2/) belonging to the French "Network of Drainage Basins" (Réseau des Bassins Versants, RBV; http://rnbv.ipgp.fr/) and Infrastructure de Recherche OZCAR (Observatoire de la Zone Critique: Applications et Recherches). The Environmental Observatory BVET is supported by Institut de Recherche pour le Développement (IRD), Centre National de la Recherche Scientifique (Institut National des Sciences de l'Univers) (CNRS/INSU), and Toulouse University. Our project benefited from funding from IRD and INSU/CNRS through the French program EC2CO (Ecosphère Continentale et Côtière) and ACI-Eau. We thank the Karnataka Forest Department and the staff of the Bandipur National Park for all the facilities and support they provided. At GET, Toulouse, we thank the staff of the thin section workshop (Fabienne de Parseval and Jean-François Mena) and Philippe de Parseval and Thierry Algouy for EPMA and SEM-BSE. We are grateful to Olivier Bruguier University Montpellier 2, France for LA-ICPMS analyses. We would like to thank Mahesh Korakoppa for helping us with the EPMA analyses at GSI, Bangalore, India.

References

Balan, E., Allard, T., Fritsch, E., Sélo, M., Falguères, C., Chabaux, F., et al. (2005). Formation and evolution of lateritic profiles in the middle Amazon basin: Insights from radiation-induced defects in kaolinite. *Geochimica Et Cosmochimica Acta*, *69*(9), 2193–2204.

Banfield, J. F., & Eggleton, R. A. (1989). Apatite replacement and rare earth mobilization, fractionation and fixation during weathering. *Clays and Clay Minerals*, *37*(2), 113–127.

Bao, Z., & Zhao, Z. (2008). Geochemistry of mineralization with exchangeable REY in the weathering crusts of granitic rocks in South China. *Ore Geology Reviews*, *33*(3–4), 519–535. http://doi.org/10.1016/j.oregeorev.2007.03.005

Barbiéro, L., Parate, H. R., Descloitres, M., Bost, A., Furian, S., Mohan Kumar, M. S., et al. (2007). Using a structural approach to identify relationships between soil and erosion in a non-anthropic forested area, South India. *Catena*, *70*(3), 313–329.

Bea, F. (1996). Residence of REE, Y, Th and U in granites and grustal protoliths: Implications for the chemistry of crustal melts. *Journal of Petrology*, *37*, 521–552.

Berger, A., Gnos, E., Janots, E., Fernandez, A., & Giese, J. (2008). Formation and composition of rhabdophane, bastnäsite and hydrated thorium minerals during alteration: Implications for geochronology and low-temperature processes. *Chemical Geology*, *254*(3–4), 238–248. https://doi.org/10.1016/j.chemgeo.2008.03.006

Berger, A., Janots, E., Gnos, E., Frei, R., & Bernier, F. (2014). Rare earth element mineralogy and geochemistry in a laterite profile from Madagascar. *Applied Geochemistry*, *41*, 218–228. https://doi.org/10.1016/j.apgeochem.2013.12.013

Bern, C. R., Yesavage, T., & Foley, N. K. (2017). Ion-adsorption REEs in regolith of the Liberty Hill pluton, South Carolina, USA: An effect of hydrothermal alteration. *Journal of Geochemical Exploration*, *172*, 29–40. https://doi.org/10.1016/j.gexplo.2016.09.009

Brantley, S. L., & Lebedeva, M. (2011). Learning to read the chemistry of regolith to understand teh Critical Zone. *Annual Review of Earth and Planetary Sciences*, *39*(1), 387–416.

Braun, J.-J., Descloitres, M., Riotte, J., Fleury, S., Barbiéro, L., Boeglin, J.-L., et al. (2009). Regolith mass balance inferred from combined mineralogical, geochemical and geophysical studies: Mule Hole gneissic watershed, South India. *Geochimica Et Cosmochimica Acta*, *73*(4), 935–961. https://doi.org/10.1016/j.gca.2008.11.013

Braun, J.-J., Pagel, M., Herbilln, A., & Rosin, C. (1993). Mobilization and redistribution of REEs and thorium in a syenitic lateritic profile: A mass balance study. *Geochimica Et Cosmochimica Acta*, *57*(18), 4419–4434. https://doi.org/10.1016/0016-7037(93)90492-f

Braun, J.-J., Pagel, M., Muller, J.-P., Bilong, P., Michard, A., & Guillet, B. (1990). Cerium anomalies in lateritic profiles. *Geochimica Et Cosmochimica Acta*, *54*(3), 781–795. https://doi.org/10.1016/0016-7037(90)90373-s

Braun, J.-J., Riotte, J., Battacharya, S., Violette, A., Prunier, J., Bouvier, V., et al. (2017). REY-Th-U solute dynamics in the critical zone: Combined influence of chemical weathering, atmospheric deposit leaching, and vegetation cycling (Mule Hole Watershed, South India). *Geochemistry, Geophysics, Geosystems*, *18*, 4409–4425. https://doi.org/10.1002/2017GC007158

Braun, J.-J., Viers, J., Dupre, B., Polve, M., Ndam, J., & Muller, J.-P. (1998). Solid/liquid REE fractionation in the lateritic system of Goyoum, East Cameroon: The implication for the present dynamics of the soil covers of the humid tropical regions. *Geochimica Et Cosmochimica Acta*, *62*(2), 273–299.

Brimhall, G. H., Christopher, J. L., Ford, C., Bratt, J., Taylor, G., & Warin, O. (1991). Quantitative geochemical approach to pedogenesis: Importance of parent material reduction, volumetric expansion and eolian influx in laterization. *Geoderma*, *51*(1–4), 51–91.

Brioschi, L., Steinmann, M., Lucot, E., Pierret, M. C., Stille, P., Prunier, J., & Badot, P. M. (2013). Transfer of rare earth elements (REE) from natural soil to plant systems: Implications for the environmental availability of anthropogenic REE. *Plant and Soil*, *366*(1–2), 143–163. https://doi.org/10.1007/s11104-012-1407-0

Buss, H. L., Mathur, R., White, A. F., & Brantley, S. L. (2010). Phosphorus and iron cycling in deep saprolite, Luquillo Mountains, Puerto Rico. *Chemical Geology*, *269*(1–2), 52–61. https://doi.org/10.1016/j.chemgeo.2009.08.001

Carignan, J., Hild, P., Mevelle, G., Morel, J., & Yeghicheyan, D. (2001). Routine analyses of trace elements in geological samples using flow injection and low pressure on-line liquid chromatography coupled to ICP-MS: A study of geochemical reference materials BR, DR-N, UB-N, AN-G and GH. *Geostandards Newsletter: The Journal of Geostandards and Geoanalysis*, *25*(2–3), 187–198.

Chabaux, F., Dequincey, O., Leveque, J.-J., Leprun, J.-C., Clauer, N., Riotte, J., & Paquet, H. (2003). Tracing and dating recent chemical transfers in weathering profiles by trace-element geochemistry and 238U—234U—230Th disequilibria: The example of the Kaya lateritic toposequence (Burkina-Faso). *Comptes Rendus Geosciences*, *335*(16), 1219–1231.

Chapman, J. B., Weiss, D. J., Shan, Y., & Lemburger, M. (2009). Iron isotope fractionation during leaching of granite and basalt by hydrochloric and oxalic acids. *Geochimica Et Cosmochimica Acta*, *73*(5), 1312–1324. https://doi.org/10.1016/j.gca.2008.11.037

Cherniak, D. J. (2010). Diffusion in accessory minerals: Zircon, titanite, apatite, monazite and xenotime. *Reviews in Mineralogy and Geochemistry*, *72*(1), 827–869. https://doi.org/10.2138/rmg.2010.72.18

Condie, K. C., Dengate, J., & Cullers, R. L. (1995). Behavior of rare earth elements in a paleoweathering profile on granodiorite in the Front Range, Colorado, USA. *Geochimica Et Cosmochimica Acta*, *59*(2), 279–294.

Coppin, F., Berger, G., Bauer, A., Castet, S., & Loubet, M. (2002). Sorption of lanthanides on smectite and kaolinite. *Chemical Geology*, *182*(1), 57–68. https://doi.org/10.1016/S0009-2541(01)00283-2

Cross, A. F., & Schlesinger, W. H. (1995). A literature review and evaluation of the Hedley fractionation—Applications to the biochemical cycle of soil phosphorus in natural ecosystems. *Geoderma*, *64*(3–4), 197–214. https://doi.org/10.1016/0016-7061(94)00023-4

Davranche, M., Grybos, M., Gruau, G., Pédrot, M., Dia, A., & Marsac, R. (2011). Rare earth element patterns: A tool for identifying trace metal sources during wetland soil reduction. *Chemical Geology*, *284*(1–2), 127–137. https://doi.org/10.1016/j.chemgeo.2011.02.014

Davranche, M., Pourret, O., Gruau, G., & Dia, A. (2004). Impact of humate complexation on the adsorption of REE onto Fe oxyhydroxide. *Journal of Colloid and Interface Science*, *277*(2), 271–279. https://doi.org/10.1016/j.jcis.2004.04.007

Dequincey, O., Chabaux, F., Clauer, N., Sigmarsson, O., Liewig, N., & Leprun, J. C. (2002). Chemical mobilizations in laterites: Evidence from trace elements and 238U-234U-230Th disequilibria. *Geochimica Et Cosmochimica Acta*, *66*(7), 1197–1210.
Duff, M. C., Coughlin, J. U., & Hunter, D. B. (2002). Uranium co-precipitation with iron oxide minerals. *Geochimica Et Cosmochimica Acta*, *66*(20), 3533–3547. https://doi.org/10.1016/S0016-7037(02)00953-5
Dupré, B., Viers, J., Dandurand, J. L., Polvé, M., Bénezeth, P., Vervier, P., & Braun, J. J. (1999). Major and trace elements associated with colloids in organic-rich river waters ultrafiltration of natural and spiked solutions. *Chemical Geology*, *160*(1–2), 63–80.
Erel, Y., Blum, J. D., Roueff, E., & Ganor, J. (2004). Lead and strontium isotopes as monitors of experimental granitoid mineral dissolution. *Geochimica Et Cosmochimica Acta*, *68*(22), 4649–4663. https://doi.org/10.1016/j.gca.2004.04.022
Finger, F., Broska, I., Roberts, M. P., & Schermaier, A. (1998). Replacement of primary monazite by apatite-allanite-epidote coronas in an amphibolite facies granite gneiss from the Eastern Alps. *American Mineralogist*, *83*(3–4), 248–258.
Foerster, H.-J. (1998a). The chemical composition of REE-Y-Th-U-rich accessory minerals in peraluminous granites of the Erzgebirge-Fichtelgebirge region, Germany; Part I, The monazite-(Ce)-brabantite solid solution series. *American Mineralogist*, *83*(3–4), 259–272. https://doi.org/10.2138/am-1998-3-409
Foerster, H.-J. (1998b). The chemical composition of REE-Y-Th-U-rich accessory minerals in peraluminous granites of the Erzgebirge-Fichtelgebirge region, Germany; Part II, Xenotime. *American Mineralogist*, *83*(11–12)(Part 1), 1302–1315. https://doi.org/10.2138/am-1998-11-1219
Gruau, G., Dia, A., Olivié-Lauquet, G., Davranche, M., & Pinay, G. (2004). Controls on the distribution of rare earth elements in shallow groundwaters. *Water Research*, *38*(16), 3576–3586. https://doi.org/10.1016/j.watres.2004.04.056
Grybos, M., Davranche, M., Gruau, G., & Petitjean, P. (2007). Is trace metal release in wetland soils controlled by organic matter mobility or Fe-oxyhydroxides reduction? *Journal of Colloid and Interface Science*, *314*(2), 490–501. https://doi.org/10.1016/j.jcis.2007.04.062
Guelke, M., von Blanckenburg, F., Schoenberg, R., Staubwasser, M., & Stuetzel, H. (2010). Determining the stable Fe isotope signature of plant-available iron in soils. *Chemical Geology*, *277*(3–4), 269–280. https://doi.org/10.1016/j.chemgeo.2010.08.010
Günther, D., & Heinrich, C. A. (1999). Enhanced sensitivity in LA-ICP-MS using helium-argon mixtures as aerosol carrier. *Journal of Analytical Atomic Spectrometry*, *14*(9), 1363–1374.
Hedley, M. J., Stewart, J. W. B., & Chauhan, B. S. (1982). Changes in inorganic and organic soil phosphorus fractions induced by cultivation practices and by laboratory incubations. *Soil Science Society of America Journal*, *46*(5), 970–976.
Hei Martin Li, Y., Winston Zhao, W., & Zhou, M.-F. (2017). Nature of parent rocks, mineralization styles and ore genesis of regolith-hosted REE deposits in South China: An integrated genetic model. *Journal of Asian Earth Sciences*, *148*, 65–95. https://doi.org/10.1016/j.jseaes.2017.08.004
Janots, E., Bernier, F., Brunet, F., Muñoz, M., Trcera, N., Berger, A., & Lanson, M. (2015). Ce(III) and Ce(IV) (re)distribution and fractionation in a laterite profile from Madagascar: Insights from in situ XANES spectroscopy at the Ce LIII-edge. *Geochimica Et Cosmochimica Acta*, *153*, 134–148. https://doi.org/10.1016/j.gca.2015.01.009
Jouquet, P., Bottinelli, N., Shanbhag, R. R., Bourguignon, T., Traore, S., & Abbasi, S. A. (2016). Termites: The neglected. *Soil Engineers of Tropical Soils, Soil Science*, *181*(3/4), 157–165. https://doi.org/10.1097/ss.0000000000000119
Jouquet, P., Chintakunta, S., Bottinelli, N., Subramanian, S., & Caner, L. (2016). The influence of fungus-growing termites on soil macro and micro-aggregates stability varies with soil type. *Applied Soil Ecology*, *101*, 117–123. https://doi.org/10.1016/j.apsoil.2016.02.001
Jouquet, P., Guilleux, N., Caner, L., Chintakunta, S., Ameline, M., & Shanbhag, R. R. (2016). Influence of soil pedological properties on termite mound stability. *Geoderma*, *262*, 45–51. https://doi.org/10.1016/j.geoderma.2015.08.020
Langmuir, D. (1978). Uranium solution-mineral equilibria at low temperatures with applications to sedimentary ore deposits. *Geochimica Et Cosmochimica Acta*, *42*(6), 547–569. https://doi.org/10.1016/0016-7037(78)90001-7
Langmuir, D., & Herman, J. S. (1980). The mobility of thorium in natural waters at low temperatures. *Geochimica Et Cosmochimica Acta*, *44*(11), 1753–1766. https://doi.org/10.1016/0016-7037(80)90226-4
Laveuf, C., & Cornu, S. (2009). A review on the potentiality of Rare Earth Elements to trace pedogenetic processes. *Geoderma*, *154*(1), 1–12. https://doi.org/10.1016/j.geoderma.2009.10.002
Ma, L., Chabaux, F., Pelt, E., Granet, M., Sak, P. B., Gaillardet, J., et al. (2012). The effect of curvature on weathering rind formation: Evidence from Uranium-series isotopes in basaltic andesite weathering clasts in Guadeloupe. *Geochimica Et Cosmochimica Acta*, *80*, 92–107. https://doi.org/10.1016/j.gca.2011.11.038
Ma, L., Jin, L., & Brantley, S. L. (2011). How mineralogy and slope aspect affect REE release and fractionation during shale weathering in the Susquehanna/Shale Hills Critical Zone Observatory. *Chemical Geology*, *290*(1–2), 31–49. https://doi.org/10.1016/j.chemgeo.2011.08.013
Maréchal, J. C., Riotte, J., Lagane, C., Subramanian, S., Kumar, C., Ruiz, L., et al. (2011). Deep groundwater flow as the main pathway for chemical outputs in a small headwater watershed. *Applied Geochemistry*, *26*, S94–S96.
Maréchal, J. C., Varma, M. R. R., Riotte, J., Vouillamoz, J. M., Mohan Kumar, M. S., Ruiz, L., et al. (2009). Indirect and direct recharges in a tropical foresetd watershed: Mule Hole, India. *Journal of Hydrology*, *364*(3–4), 272–284.
Middleton, A. W., Förster, H.-J., Uysal, I. T., Golding, S. D., & Rhede, D. (2013). Accessory phases from the Soultz monzogranite, Soultz-sous-Forêts, France: Implications for titanite destabilisation and differential REE, Y and Th mobility in hydrothermal systems. *Chemical Geology*, *335*, 105–117. https://doi.org/10.1016/j.chemgeo.2012.10.047
Naqvi, S. M., & Rogers, J. W. (1987). *Precambrian geology of India* (223 pp.). New York: Clarendon Press.
Nesbitt, H. W., & Markovics, G. (1997). Weathering of granodiorite crust, long-term storage of elements in weathering profiles, and petrogenesis of siliclastic sediments. *Geochimica Et Cosmochimica Acta*, *61*(8), 1653–1670.
Oh, N.-H., & Richter, D. D. (2005). Elemental translocation and loss from three highly weathered soil-bedrock profiles in the southeastern United States. *Geoderma*, *126*(1–2), 5–25.
Panahi, A., Young, G. M., & Rainbird, R. H. (2000). Behavior of major and trace elements (including REE) during Paleoproterozoic pedogenesis and diagenetic alteration of an Archean granite near Ville Marie, Québec, Canada. *Geochimica Et Cosmochimica Acta*, *64*(13), 2199–2220. https://doi.org/10.1016/S0016-7037(99)00420-2
Pearce, N. J., Perkins, W. T., Westgate, J. A., Gorton, M. P., Jackson, S. E., Neal, C. R., & Chenery, S. P. (1997). A compilation of new and published major and trace element data for NIST SRM 610 and NIST SRM 612 glass reference materials. *Geostandards Newsletter: The Journal of Geostandards and Geoanalysis*, *21*(1), 115–144.
Poitrasson, F., Chenery, S., & Shepherd, T. J. (2000). Electron microprobe and LA-ICP-MS study of monazite hydrothermal alteration: Implications for U-Th-Pb geochronology and nuclear ceramics. *Geochimica Et Cosmochimica Acta*, *64*(19), 3283–3297. https://doi.org/10.1016/S0016-7037(00)00433-6
Pourret, O., Davranche, M., Gruau, G., & Dia, A. (2007a). Organic complexation of rare earth elements in natural waters: Evaluating model calculations from ultrafiltration data. *Geochimica Et Cosmochimica Acta*, *71*(11), 2718–2735. https://doi.org/10.1016/j.gca.2007.04.001

Pourret, O., Davranche, M., Gruau, G., & Dia, A. (2007b). Rare earth elements complexation with humic acid. *Chemical Geology*, *243*(1–2), 128–141. https://doi.org/10.1016/j.chemgeo.2007.05.018

Riotte, J., Meunier, J. D., Zambardi, T., Audry, S., Barboni, D., Anupama, K., et al. (2018). Processes controlling silicon isotopic fractionation in a forested tropical watershed: Mule Hole Critical Zone Observatory (Southern India). *Geochimica Et Cosmochimica Acta*, *228*, 301–319. https://doi.org/10.1016/j.gca.2018.02.046

Riotte, J., Ruiz, L., Audry, S., Sekhar, M., Mohan Kumar, M. S., Siva Soumya, B., & Braun, J. J. (2014). Impact of vegetation and decennial rainfall fluctuations on the weathering fluxes exported from a dry tropical forest (Mule Hole). *Procedia Earth and Planetary Science*, *10*, 34–37. https://doi.org/10.1016/j.proeps.2014.08.007

Rudnick, R., & Gao, S. (2003). Composition of the continental crust. *Treatise on Geochemistry*, *3*, 1–64.

Ruiz, L., Varma, M. R. R., Kumar, M. S. M., Sekhar, M., Maréchal, J.-C., Descloitres, M., et al. (2010). Water balance modelling in a tropical watershed under deciduous forest (Mule Hole, India): Regolith matric storage buffers the groundwater recharge process. *Journal of Hydrology*, *380*(3–4), 460–472. https://doi.org/10.1016/j.jhydrol.2009.11.020

Sanematsu, K., Kon, Y., & Imai, A. (2015). Influence of phosphate on mobility and adsorption of REEs during weathering of granites in Thailand. *Journal of Asian Earth Sciences*, *111*, 14–30. https://doi.org/10.1016/j.jseaes.2015.05.018

Sanematsu, K., Kon, Y., Imai, A., Watanabe, K., & Watanabe, Y. (2013). Geochemical and mineralogical characteristics of ion-adsorption type REE mineralization in Phuket, Thailand. *Mineralium Deposita*, *48*(4), 437–451. https://doi.org/10.1007/s00126-011-0380-5

Schwertmann, U., & Pfab, G. (1996). Structural vanadium and chromium in lateritic iron oxides: Genetic implications. *Geochimica Et Cosmochimica Acta*, *60*(21), 4279–4283. https://doi.org/10.1016/S0016-7037(96)00259-1

Sengupta, D., & Van Gosen, B. S. (2016). Placer-type rare earth element deposits. *Reviews in Economic Geology*, 18, 81–100.

Seydoux-Guillaume, A.-M., Montel, J.-M., Bingen, B., Bosse, V., de Parseval, P., Paquette, J.-L., et al. (2012). Low-temperature alteration of monazite: Fluid mediated coupled dissolution–precipitation, irradiation damage, and disturbance of the U–Pb and Th–Pb chronometers. *Chemical Geology*, *330–331*, 140–158. https://doi.org/10.1016/j.chemgeo.2012.07.031

Shadakshara Swamy, N., Jayananda, M., & Janardhan, A. S. (1995). Geochemistry of Gundlupet gneisses, Southern Karnataka: A 2.5 Ga old reworked sialic crust. In M. Yoshida, M. Santosh & A. T. Rao (Eds.), *India as a fragment of East Gondwana* (pp. 87–97). Gondwana Research Group.

Simandl, G. J. (2014). Geology and market-dependent significance of rare earth element resources. *Mineralium Deposita*, *49*(8), 889–904. https://doi.org/10.1007/s00126-014-0546-z

Singh, P., & Rajamani, V. (2001). REE geochemistry of recent clastic sediments from the Kaveri floodplains, southern India: Implication to source area weathering and sedimentary processes. *Geochimica Et Cosmochimica Acta*, *65*(18), 3093–3108.

Smith, M. P., Moore, K., Kavecsánszki, D., Finch, A. A., Kynicky, J., & Wall, F. (2016). From mantle to critical zone: A review of large and giant sized deposits of the rare earth elements. *Geoscience Frontiers*, *7*(3), 315–334. https://doi.org/10.1016/j.gsf.2015.12.006

Stille, P., Steinmann, M., Pierret, M. C., Gauthier-Lafaye, F., Chabaux, F., Viville, D., et al. (2006). The impact of vegetation on REE fractionation in stream waters of a small forested catchment (the Strengbach case). *Geochimica Et Cosmochimica Acta*, *70*(13), 3217–3230. https://doi.org/10.1016/j.gca.2006.04.028

Su, N., Yang, S., Guo, Y., Yue, W., Wang, X., Yin, P., & Huang, X. (2017). Revisit of rare earth element fractionation during chemical weathering and river sediment transport. *Geochemistry, Geophysics, Geosystems*, *18*, 935–955. https://doi.org/10.1002/2016GC006659

Summerfield, M. A. (1991). *Global geomorphology. An introduction to the study of landforms* (537 pp.). Upper Saddle River, NJ: Prentice Hall.

Taboada, T., Martínez Cortizas, A., García, C., & García-Rodeja, E. (2006). Uranium and thorium in weathering and pedogenetic profiles developed on granitic rocks from NW Spain. *Science of the Total Environment*, *356*(1–3), 192–206. https://doi.org/10.1016/j.scitotenv.2005.03.030

Tarantola, A., & Valette, B. (1982). Generalized nonlinear inverse problems solved using the least squares criterion. *Reviews of Geophysics and Space Physics*, *20*(2), 219–232.

Taunton, A. E., Welch, S. A., & Banfield, J. F. (2000). Microbial controls on phosphate and lanthanide distributions during granite weathering and soil formation. *Chemical Geology*, *169*(3–4), 371–382. https://doi.org/10.1016/S0009-2541(00)00215-1

Taylor, S. R., & McLennan, S. M. (1985). *The continental crust: Its composition and evolution—An examination of the geochemical record preserved in sedimentary rocks* (312 pp.). Oxford, UK: Blackwell.

Thompson, A., Amistadi, M. K., Chadwick, O. A., & Chorover, J. (2013). Fractionation of yttrium and holmium during basaltic soil weathering. *Geochimica Et Cosmochimica Acta*, *119*, 18–30. https://doi.org/10.1016/j.gca.2013.06.003

Tyler, G. (2004). Rare earth elements in soil and plant systems—A review. *Plant and Soil*, *267*(1–2), 191–206. https://doi.org/10.1007/s11104-005-4888-2

Van Achterberg, E., Ryan, C. G., Jackson, S. E., & Griffin, W. (2001). Data reduction software for LA-ICP-MS. In E. Sylvester (Ed.), *Laser ablation ICP-MS in the Earth Science* (pp. 239–243). Québec City, QC: Mineralogical Association of Canada.

Vazquez-Ortega, A., Huckle, D., Perdrial, J., Amistadi, M. K., Durcik, M., et al. (2016). Solid-phase redistribution of rare earth elements in hillslope pedons subjected to different hydrologic fluxes. *Chemical Geology*, *426*, 1–18. https://doi.org/10.1016/j.chemgeo.2016.01.001

Vázquez-Ortega, A., Perdrial, J., Harpold, A., Zapata-Ríos, X., Rasmussen, C., McIntosh, J., et al. (2015). Rare earth elements as reactive tracers of biogeochemical weathering in forested rhyolitic terrain. *Chemical Geology*, *391*, 19–32. https://doi.org/10.1016/j.chemgeo.2014.10.016

Viers, J., Dupre, B., Polve, M., Schott, J., Dandurand, J. L., & Braun, J. J. (1997). Chemical weathering in the drainage basin of a tropical watershed (Nsimi-Zoetele site, Cameroon): Comparison between organic poor and organic rich waters. *Chemical Geology*, *140*(3–4), 181–206.

Viers, J., & Wasserburg, G. J. (2004). Behavior of Sm and Nd in a lateritic soil profile. *Geochimica Et Cosmochimica Acta*, *68*(9), 2043–2054.

Violette, A., Godderis, Y., Marechal, J.-C., Riotte, J., Oliva, P., Kumar, M. S. M., et al. (2010a). Modelling the chemical weathering fluxes at the watershed scale in the Tropics (Mule Hole, South India): Relative contribution of the smectite/kaolinite assemblage versus primary minerals. *Chemical Geology*, *277*(1–2), 42–60. https://doi.org/10.1016/j.chemgeo.2010.07.009

Violette, A., Riotte, J., Braun, J.-J., Oliva, P., Marechal, J.-C., Sekhar, M., et al. (2010b). Formation and preservation of pedogenic carbonates in South India, links with paleo-monsoon and pedological conditions: Clues from Sr isotopes, U–Th series and REEs. *Geochimica Et Cosmochimica Acta*, *74*(24), 7059–7085. https://doi.org/10.1016/j.gca.2010.09.006

Wiederhold, J. G., Teutsch, N., Kraemer, S. M., Halliday, A. N., & Kretzschmar, R. (2007). Iron isotope fractionation in oxic soils by mineral weathering and podzolization. *Geochimica Et Cosmochimica Acta*, *71*(23), 5821–5833. https://doi.org/10.1016/j.gca.2007.07.023

Xu, C., Kynický, J., Smith, M. P., Kopriva, A., Brtnický, M., Urubek, T., et al. (2017). Origin of heavy rare earth mineralization in South China. *Nature Communications*, *8*, 14598. https://doi.org/10.1038/ncomms14598.

Zaharescu, D. G. (2017). Ecosystem composition controls the fate of rare earth elements during incipient soil genesis, *Scientific Reports*, *7*, 43208. https://doi.org/10.1038/srep43208